Numerical Simulations and Machine Learning Modeling of Magnetic Systems

Zhongzheng Tian

Charlottesville, VA

B.S. in Mathematics and B.S. in Physics

University of Maryland, College Park

August, 2015

A Dissertation Presented to

the Graduate Faculty of the University of Virginia

in Candidacy for the Degree of

Doctor of Philosophy

Department of Physics

University of Virginia

November, 2021

Acknowledgement

First, I would like to express my gratitude to my Ph.D. advisor, Prof. Gia-Wei Chern. Without his guidance, insight, and continuous support, I could not possibly have completed this work.

I would also like to thank the other members of my defense committee, Prof. Israel Klich, Prof. Bellave Shivaram, and Prof. Sergei Egorov, for their support and for their suggestions for improving my research.

Moreover, I would like to express my appreciation to the faculty members as well as to my friends in the Physics Department. Their support, both in life and in academics, has been invaluable to me. I also thank my friend Allan Megill for his help with improving my English.

Finally, I need to thank my mother. Without her encouragement in the past years, it would have been impossible for me to have completed my Ph.D. study.

Contents

List of Figures

Chapter 1

Introduction

Magnetism was discovered by the ancient Chinese and ancient Greeks in the early years of human civilization. However, its microscopic mechanism was not fully understood until the 20th century when Heisenberg explained ferromagnetism by considering it an effect of quantum mechanics. Heisenberg constructed a model that incorporated exchange interactions between localized spins, in which the exchange interaction is led by the Coulomb interaction coupling with the Pauli exclusion principle. The model is given by the following Hamiltonian:

$$\mathcal{H} = \frac{1}{2}\sum_{ij} J_{ij}\mathbf{S}_i \cdot \mathbf{S_j}, \tag{1.1}$$

where J_{ij} are the exchange couplings between spins. Evidently, the negative values of J would lead the ground state of the system to be ferromagnetic. On the other hand, it was first pointed out by Louis Néel that a positive value of J could lead the system to be antiferromagnetic. In an antiferromagnetic state, the nearest neighbor spins are anti-parallel to each other. This can be

illustrated by a Heisenberg model with nearest neighbour exchange J on a simple cubic lattice. The system is bipartite: it can be separated into two non-overlapping sublattices in which spins of one sublattice have the nearest neighbors from the other sublattice. The ground states of the system are two-sublattice antiferromagnetic states, where spins from one sublattice have same directions while the spins from the other one point oppositely. The model has a symmetry that these states are unique up to global spin rotations.

1.1 Frustrated Magnetism

However, nowadays there are a type of magnets which can possibly evade the antiferromagnetic order. They are posing much higher challenges than the simple anti-ferromagnetism both in theories and in experiments. These so-called frustrated magnets are named in contrast to the conventional ordered "unfrustrated" magnets. Frustrated magnetism refers to competing interactions that cannot be simultaneously satisfied [1, 2], and it was first introduced by Wannier in the 1950s. Wannier showed a 2-dimensional Ising system with triangular lattices that has a large degeneracy of ground states, as exemplified by three spins antiferromagnetically coupled to each other on an equilateral triangle. Frustrated magnets attract extensive interest because they can possibly destruct the antiferromagnetic order. These systems tend to have many low-frequency modes. The excitations can reduce the ordered moment effectively and they are thermally occupied at low temperature. Moreover, the frustration could lead to many different kinds of classical ground states and

could suppress the Néel temperature T_N to zero, where the Néel temperature describe a temperature limit at which a paramagnetic state transfers into an antiferromangetic state, or vice versa.

As a way of evading antiferromagnetic order, frustration has been widely studied in models with competing nearest neighbor (NN) and next nearest neighbor (NNN) interactions. A well-known example is the competition between NN J_1 and NNN J_2 antiferromagnetic exchange couplings in bipartite lattices (figure 1.1 (left and center)). When the ratio $J_2/J_1 < 0.5$, neighboring spins are anti-parallel, forcing the second nearest neighbors to be ferromagnetic and resulting in frustration of interaction J_2. On the other hand, for $J_2/J_1 > 0.5$, neighboring spins are parallel, leading the second nearest neighbors to be antiferromagnetic and resulting in frustration of half of J_1 interactions. The special point $J_2 = J_1/2$ is particularly interesting since alternative classical states are degenerate and thus the frustration is maximized [3].

Besides the models of the J_1-J_2 type, there is another intriguing kind of frustrated magnetic system in which the structure alone can destabilize the antiferromagnetic order. This is called geometrical frustration. To give an illustrative example of geometrical frustration, consider the structure depicted in figure 1.1 (right). The system has classical Heisenberg spins at vertices of two neighboring triangles with nearest neighbor antiferromagnetic interactions. The ground states of the system are the configurations where co-planar spins in each triangle have a relative angle of $2\pi/3$. In this case, the relative rotations of the spin planes of the two triangles about the axis, which is aligned in the orientation of the common spin, lead to an accidental degeneracy in the ground

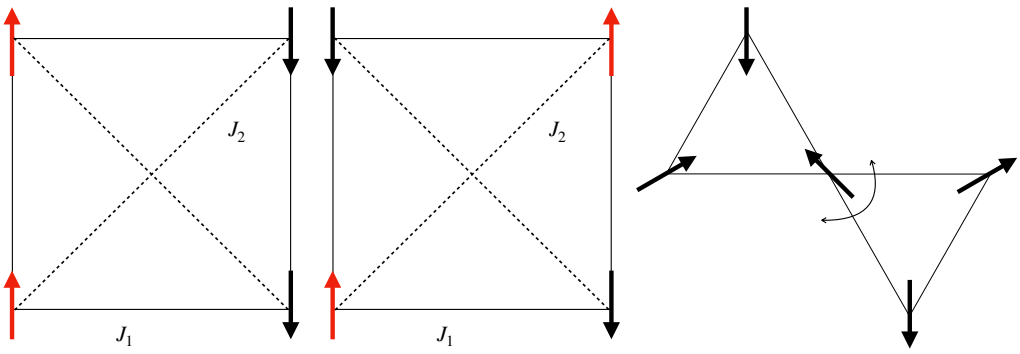

Figure 1.1: (left and center) J_1-J_2 model shows ground state spin configurations for conditions: $J_2/J_1 > 0.5$ on the left and $J_2/J_1 < 0.5$ on the right. (Right) Heisenberg spins at the vertices of two connecting triangles.

states.

If we extend the features of this simple system of two corner-sharing triangles to a periodic lattice, we can construct frustrated clusters on non-bipartite lattices made of corner-sharing arrangements. In these clusters, local magnetized moments have exchange interactions equal in between and they are located at the vertices connecting triangles. A typical example of these clusters is the kagome lattice (1.2 (left)). If we extend the similar concept to 3-dimensional lattice, we could build pyrochlore lattice made of corner-sharing tetrahedrons (1.2 (right)). Both types of examples contain a macroscopic number of triangular loops, are representative platforms for highly frustrated magnets. Their ground state degeneracy scales exponentially with the system size. The frustration is so severe that spins remain disordered at temperatures

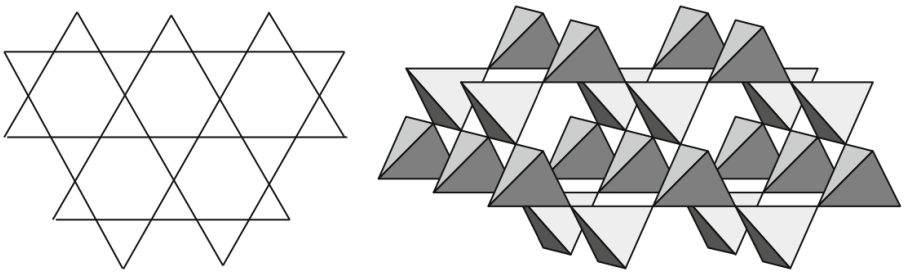

Figure 1.2: (left) Kagome lattice. (Right) Pyrochlore lattice. The figure is extracted from the book *Introduction to Frustrated Magnetism* [4].

well below the exchange energy scale and a macroscopic degeneracy develops in the classical ground state [4, 5, 6, 7, 8].

The most distinguishable feature of frustrated magnets is perhaps their abnormal dependence on of magnetic susceptibility on temperature T of χ. Consider the Curie-Weiss law:

$$\chi^{-1} \propto T - \Theta_{CW} \tag{1.2}$$

where the Curie-Weiss constant Θ_{CW} distinguishes the sign and strength of interactions. For unfrustrated magnets, χ^{-1} usually has a linear relation against T at high temperatures, and a sharp cusp in χ^{-1} would appear at the temperature $T_N \sim \Theta_{CW}$. The cusp indicates that the system releases a large amount of entropy, and that it is transiting from a paramagnetic state to a magnetic ordering state upon cooling. However, for frustrated magnets, such a sharp cusp would not be observed in systems, since they do not form a conventional long-range magnetic order even at temperatures below Θ_{CW}. The paramagnetic phase survives and becomes highly correlated at temperatures $T \ll \Theta_{CW}$.

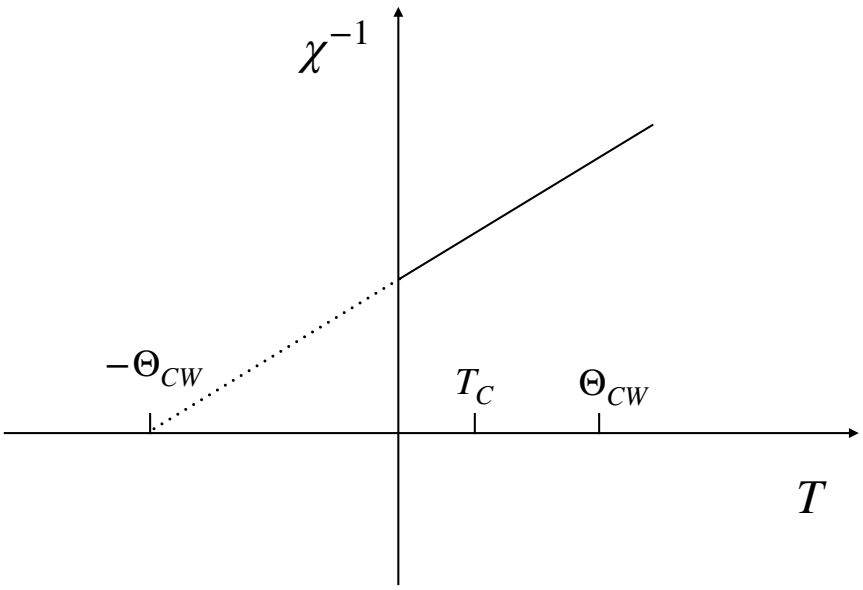

Figure 1.3: χ vs T, the critical behavior of frustrated magnets.

Nevertheless, the spin ordering, or freezing, may possibly appear at a lower temperature T_C, which will result in a large value of the ratio $f := \Theta_{CW}/T_C$ (1.3). A large value of this operational definition f suggests that the system has local degrees of freedom that fluctuate without the system leaving the ground state.

In short, frustrated magnets can have macroscopic ground state degeneracy and suppresses long range order. In this thesis, we will study a new type of frustration with the anisotropic exchange. Also named as Γ interaction, this new type of frustration is shown to play an important role in compounds such as $RuCL_3$. Microscopically, the Γ interaction originates from spin-orbit

coupling, and is often viewed as the symmetric counterpart of the antisymmetric Dzyaloshinski-Moriya interaction. Our research has as one of its foci this so-called Γ model. Previous study on the model demonstrated a thermal order-by-disorder in the system leads to a phase transition into a new spin liquid phase, that has a hidden long range flux order. Our goal in this study is to continue the investigation of the flux order when an external field is applied on this system, until a new magnetic ordering is observed in the high field. We further explore behaviors of the system when thermal fluctuation, accompanied with the external field, lifts the O(2) symmetry of the mean field magnetic order, wherein we observe a Kosterlitz–Thouless phase transition.

Our study also focuses on a system with disordered exchange interactions. Systems of this type has randomly distributed, rather than periodically arranged, exchange interactions. The interplay of disorder and frustration therein may lead the system to exotic states such as spin glass from spin liquid. Spin liquid has strong fluctuations that prevent the system from forming long range order at temperatures as low as zero.

By introducing a quenched disorder, magnets with well-defined orders in ground states may have frustrated pairwise interactions. When the disorder is big enough to shatter the coherent propagation of ordering through the system, a glass transition emerges in the system. However, for geometrical frustrations, magnets could form spin liquid order if the frustration were somehow maximized. With the introduction of quenched disorder, the flat energy surface of the frustrated magnet would be replaced by a rugged energy landscape. Spins in the system simultaneously freeze at a temperature below the typical energy

variation in such an energy landscape. This temperature is defined as T_f. In our study, we consider the disorder in interactions in the disordered J_1-J_2 system as a possible origin of spin glass, and investigate how does it spur the glass transition of the system in low temperature.

1.2 Machine Learning Assisted Studies of Magnetic Systems

Machine learning is a fast advancing technique that has reshaped many industries. Due to the ability of deep neural networks to learn both patterns and mapping between raw data and desired quantities, users are able to extract essential information from large amounts of complex data, which previously would have been unfeasible. Not surprisingly, machine learning has entered such fields of physics research as density functional theory (DFT), structure identifications, quantum molecular dynamics [9, 10, 11, 12, 13, 14], etc. For example, DFT computations rely on an expensive self-consistent field procedure of the Kohn-Sham (KS) equation to extract the functional derivatives of exchange correlation energy. An alternative approach could use a neural network (NN) to directly approximate energy functionals from atomic configurations, thus bypass the costly self-consistent computation cycles of KS equations [15, 16].

During the past decades, machine learning techniques have been applied for structure identifications and energy estimations in numerous models, ranging from simple Ising model to Hubbard model and topology models [17]. In

their pioneering work, Carrasquilla and Melko, Convolutional Neural Networks (CNN) were employed to study the Ising model, and successfully showed CNN can accurately predict extensive physical parameters such as energy density and phase transitions [18]. In their model, the way NN learn the mapping between the system configuration and physical parameters is relatively primitive that entire configurations of Ising systems need to befed into NN as as training samples. Despite the machine learning's tremendous success in those physics studies, scalability could be a limiting factor preventing the progress in such area. In these studies, the trained neural networks cannot be applied for the predictions on arbitrary system sizes. This is because in these neural network models, optimized weights and biases work exclusively for a fixed number of input nodes corresponding to the complete system configuration. If a prediction needs to be made for a different system size other than training samples', the neural network must be rebuilt according the size of system. In other words, these neural network models do not possess a scalability for the same physical systems in different sizes.

Similar problems have been encountered in the studies of *Ab-Inito* molecular dynamics. Behler and Parrinello proposed a new neural network framework to deal with configurations of different sizes. The main idea underlying the framework is to constitute the total energy E of the system as a sum of contributions of each atom E_i [16]. The key concept relating to the reason of summing over local energy contributions is locality. In short, the principle of locality states that an object is directly influenced only by its immediate surroundings. Thus when the locality is relatively small, the neural network

is more possible to learn the global parameters by local segments of system configurations. Moreover, to better describe the energetically relevant local environment of each atom, a series of descriptors are introduced to transform the Cartesian coordinates of each atom into a set of symmetry functions values in the framework. The purpose of implementing descriptors is to respect the permutation symmetry such that the total energy is invariant with respect to interchange of spins, as well as to the translational and rotational symmetries. These symmetry functions (descriptors) values are then sent into the NN as training samples. The framework provides a so-called subnet S_i for each atom, which would yield the energy contribution E_i after being optimized. All of the subnets share the same values of weights and biases to ensure permutation symmetry. Through the repeated computations on the training dataset in this way, the neural network model can learn the mapping between the local structures relevant to each atom and the total energy related to the whole system. In this way, the neural network can be transferable to predict energy for systems of arbitrary sizes.

Also, study in chemical science used a similar scheme to apply neural networks to Ising system configurations. Their model sliced the configurations of Ising systems into square shape segments that are considered to cover the locality of desired quantities, such as energy density. The neural network was then trained repeatedly with these square segments as input until the total energy of the system is summed. Similarly, the neural network trained with a certain size of Ising system configuration can be applied to predict systems of arbitrary sizes. This so called Extensive Deep Neural Network (EDNN) takes

advantage of length scale embedded in training data, but it does not learn lengthy scale an does not clarify what impact is followed by such applications [19].

Since the scalability rests on the foundation of an appropriate treatment of locality, an interesting question arise so: how does locality, or the length scale, influence the performance of the neural network? Evidently, prediction accuracy deteriorates when the size of input data becomes smaller. One may speculate that the prediction accuracy would break down when the size of input fails to contain the correlation length. Therefore, it is necessary to perform a numerical investigation to elucidate how the correlation length impacts the prediction accuracy. In our study, we define the size of square segmental input to be the focal length and use it as a measurement of correlation length.

In this study, we investigated the various scenarios of Ising systems where convolutional or fully connected neural networks can be applied. We found a systematic deviation around the phase transition point in the curve of energy prediction compared with energy values extracted from Monte-Carlo simulation. A neural network performing well in lower and higher temperatures may overestimate or underestimate the energy density around the phase transition due to the rapidly increase in correlation length. In order to explain such the deviation, we investigated the relation between NN's accuracy of phase classifications and sizes of focal length. Finally, we carried out a quantitative study that attempted to find the power law decay relation between focus size and phase predicting accuracy.

1.3 Thesis Layout

The thesis consists of topics listed in the following content, and the theis is laid out in this order:

Honeycomb-lattice Γ *Model in a Magnetic Field.* We show that a magnetic field in the high-symmetry direction lifts the macroscopic classical ground-state degeneracy of the honeycomb Γ model and induces a long-range magnetic order. An intriguing $\sqrt{3} \times \sqrt{3}$ magnetic order is selected by magnetic field for the antiferromagnetic interaction. We also show that, at high fields, the breaking of the ground-state Z_6 symmetry is through two Berezinskii-Kosterlitz-Thouless transitions that enclose a critical XY phase.

Disordered J_1-J_2 *Model.* We present a numerical study of the disodered J_1-J_2 system. In the study, we find a glass transition of the disordered J_1-J_2 system modeled for a special compound at $T_f = 0$, and derive corresponding critical exponents. Moreover, we conduct simulations to construct its dynamic structure factor, in which a coexistence of spin-wave like dispersion and non-coherent excitations can be observed. We further explain spin-wave excitation by the Halperin-Saslow theory.

Machine learning Phases of Matter on Ising Model. In the study, we present a transferable machine learning framework that can be applied to analyze system configurations of arbitrary sizes for a certain kind of physics model. The neural network model can make accurate predictions of extensive parameters such as phase, energy and etc. We show the neural network used in this research has a limitation that systematic deviations of the energy prediction results are found around the phase transition temperature. We further infer

the limitation is related to the locality of these extensive parameters. Finally, we extract a critical exponent to describe the collapse of phase prediction accuracy curves over the input focus sizes.

Chapter 2

Gamma Model Subjected to an External Field

Frustrated interactions in Mott insulators with unquenched orbital degrees of freedom have aroused our great interests. A salient feature of this type of systems is that orbital exchange interactions are highly directional, as represented by quantum compass or quantum 120° models. Expressing the orbital variables in terms of pseudo-spins, this anisotropy suggests that different spin-components are involved in exchange interactions along different spatial directions. Recently, a new type of frustration emerges, in which interaction-energy between neighboring pairs along different orientations cannot be simultaneously minimized. Lattice geometry contributes to the orbital frustration through its interplay with the anisotropic orbital exchange, instead of the loop-induced frustration for conventional geometrically frustrated magnets. Indeed, several highly frustrated orbital models are defined on bipartite lattices. More-

over, similar to geometrically frustrated systems, large accidental degeneracy, sometimes of macroscopic scale, results from orbital frustration.

Magnetic frustration that involves anisotropic exchange coupling has recently attracted enormous research interests. These materials often contain 4d or 5d transition metal elements, and are Mott insulators with strong spin-orbit coupling. In these compounds, the localized spin and orbital degrees of freedom are entangled to each other by the relativistic spin-orbit interaction. The resultant composite degree of freedom, which can be viewed as an effective spin variable, preserves the orbital character and is spatially highly anisotropic. One particular example is the spin-1/2 Kitaev model with Ising-like interactions involving different spin components on the three distinct nearest-neighbor bonds on the honeycomb lattice. Such anisotropic spin-spin interactions are frustrated as evidenced by the macroscopic ground-state degeneracy in the $S \mapsto \infty$ classical limit. Remarkably, the spin-1/2 Kitaev model is exactly solvable and exhibits a quantum spin-liquid ground state with fractionalized excitations. Originally proposed as a toy model for fractionalized excitations and topological quantum computing, it was later pointed out that Kitaev-type exchange interaction can be realized in 4d transition metal compounds such as A_2IrO_3 (A = Li, Na) and $RuCl_3$. However, other spin-spin interactions, including the isotropic Heisenberg exchange, compete with the Kiatev interaction and often destabilize the spin liquid phase. There has been a considerable amount of efforts devoted to the study of general anisotropic pseudo-spin interactions in spin-orbital coupled Mott insulators.

The recent renewed interest in such systems was partly generated by the

advent of Kitaev materials [20, 21, 22, 23]. Originally proposed as a toy model for fractionalized excitations and topological quantum computing [24], it was later pointed out that Kitaev-type exchange interaction can be realized in d^5 transition metal compounds such as A_2IrO_3 and $RuCl_3$ [25, 26, 27]. The possibility that Kitaev materials might host the elusive quantum spin liquids has generated a flurry of experimental efforts on related compounds and their characterizations. However, other spin-spin interactions, including the isotropic Heisenberg exchange, compete with the Kitaev interaction and often destabilize the spin liquid phase. Considerable efforts have thus been devoted to the study of general anisotropic pseudo-spin interactions in spin-orbit coupled Mott insulators [28, 29, 30, 31, 32, 33].

2.1 Γ Model and its Hamiltonian

In particular, the anisotropic exchange, also called the Γ interaction [34] is shown to play an important role in compounds such as $RuCl_3$. The Γ model on the honeycomb lattice is defined as [35, 36, 37]

$$\mathcal{H} = \Gamma \sum_{\gamma} \sum_{\langle ij \rangle \| \gamma} (S_i^{\alpha} S_j^{\beta} + S_i^{\beta} S_j^{\alpha}) - \mathbf{H} \cdot \sum_i \mathbf{S}_i, \tag{2.1}$$

where (α, β, γ) are permutations of (x, y, z). We have also included the Zeeman coupling to a magnetic field $\mathbf{H} = H\hat{\mathbf{n}}$ in the $\hat{\mathbf{n}} \parallel [111]$ direction. The honeycomb Γ model is a highly frustrated spin system which supports a novel classical spin-liquid ground state [35]. The extensive degeneracy associated with the classical ground state is characterized by an emergent global O(3)

rotational symmetry and a local Z_2 gauge-like symmetry [35]. While the local Ising-gauge symmetry cannot be spontaneously broken [38], the continuous O(3) degeneracy is lifted by quantum or thermal fluctuations [35, 36]. Interestingly, the spontaneous breaking of the O(3) symmetry actually corresponds to a breaking of lattice translation symmetry. Through the order-by-disorder mechanism, fluctuations thus induce a sharp phase transition below which an exotic spin liquid with a hidden $\sqrt{3} \times \sqrt{3}$ plaquette order emerges as the semiclassical ground state [36].

In this paper, we study the effect of magnetic field on the semiclassical honeycomb Γ model. The large degeneracy of frustrated magnets renders them susceptible to perturbations brought about by the magnetic field. Indeed, novel field-induced phases such as magnetization plateau and even spin liquid have been reported in both geometrically frustrated magnets [39, 40, 41, 42, 43, 44, 45, 46, 47, 48] and Kitaev spin models [49, 50, 51, 52, 53, 54, 55, 56, 57, 58, 59, 60]. In our case, the extensive ground-state degeneracy of the classical Γ-model is lifted by field along the high-symmetry [111] direction. For the ferromagnetic case with $\Gamma < 0$, the polarized state with spins aligning with the field direction is selected by the field since this particular ferromagnetic state happens to be one of the ground state of the zero-field Γ model [35].

2.2 Stability analysis

The antiferromagnetic Γ model, on the other hand, remains frustrated in the presence of magnetic field. To obtain the structure of possible field-induced

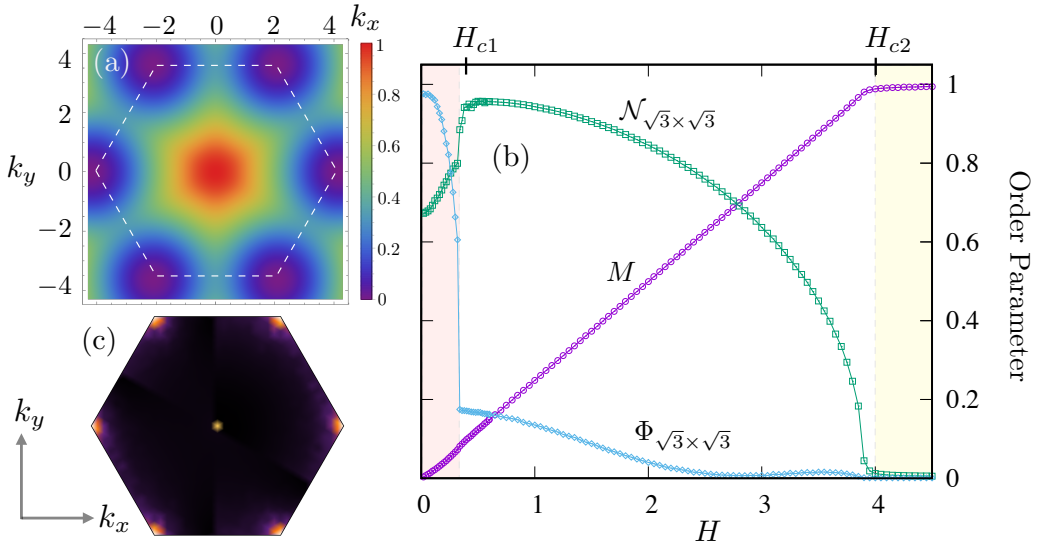

Figure 2.1: (a) Density plot in $\boldsymbol{k}$-space of the minimum eigen-energy of the fluctuation interaction E_2. The dashed line marks the boundary of the first Brillouin zone. (b) Monte Carlo simulation results at temperature $T = 0.01\Gamma$ showing the field dependence of $\sqrt{3} \times \sqrt{3}$ magnetic order $\mathcal{N}_{\sqrt{3}\times\sqrt{3}}$, plaquette flux order $\Phi_{\sqrt{3}\times\sqrt{3}}$, and magnetization M. (c) The static structure factor of the intermediate state from Monte Carlo simulation at $H = 2\Gamma$ and $T = 0.01\Gamma$.

order, we investigate the stability of the polarized state at large H.We expect at high field limit $H = 4\Gamma$, all spins are polarized to the direction parallel to the unit vector $\hat{n} = \hat{e} = \frac{1}{\sqrt{3}}[1,1,1]$. Here we define two unit vectors $\hat{e}_a = (\hat{e}_x + \hat{e}_y - 2\hat{e}_z)/\sqrt{6}$ and $\hat{e}_b = (\hat{e}_y - \hat{e}_x)/\sqrt{2}$, where $\hat{e}_x$, $\hat{e}_y$ and $\hat{e}_z$ are three unit vectors in the three cubic axes. Evidently $\hat{e}_a$, $\hat{e}_b$ and $\hat{n}$ constitute an orthogonal basis. Evidently, spins will de-polarize from $\hat{n}$ direction once the field decreases to a certain level. By the definitions of $\hat{e}_a$ and $\hat{e}_b$, we can decompose the spin field as:

$$\boldsymbol{S}_i = \sqrt{1 - |\boldsymbol{\sigma}_i|^2}\hat{n} + \sigma_i^a \boldsymbol{e}_a + \sigma_i^b \boldsymbol{e}_b \tag{2.2}$$

where $\boldsymbol{e}_a = (\boldsymbol{e}_x + \boldsymbol{e}_y - 2\boldsymbol{e}_z)/\sqrt{6}$ and $e_b = (\boldsymbol{e}_y - 2\boldsymbol{e}_x)/\sqrt{2}$. Therein, each component of the spin can be expressed as:

$$S_i^\gamma = \frac{1}{\sqrt{3}}\sqrt{1 - |\boldsymbol{\sigma}_i|^2} + \sqrt{\frac{2}{3}}\boldsymbol{\sigma}_i \cdot \boldsymbol{t}^\gamma \tag{2.3}$$

where $\boldsymbol{t}^x = (\frac{1}{2}, -\frac{\sqrt{3}}{2})$, $\boldsymbol{t}^y = (\frac{1}{2}, \frac{\sqrt{3}}{2})$, and $\boldsymbol{t}^z = (-1, 0)$. Without loss of generality, we assume the magnitude of S to be 1. Expand the spin interaction $S_i^\alpha S_j^\beta$ to second order in σ:

$$\begin{aligned} S_i^\alpha S_j^\beta = &\frac{1}{3}\left(1 - \frac{1}{2}|\boldsymbol{\sigma}_i|^2 - \frac{1}{2}|\boldsymbol{\sigma}_j|^2\right) \\ &+ \frac{\sqrt{2}}{3}\left(\boldsymbol{\sigma}_i \cdot \boldsymbol{t}^\alpha + \boldsymbol{\sigma}_j \cdot \boldsymbol{t}^\beta\right) + \frac{2}{3}\left(\boldsymbol{\sigma}_i \cdot \boldsymbol{t}^\alpha\right)\left(\boldsymbol{\sigma}_j \cdot \boldsymbol{t}^\beta\right) \end{aligned} \tag{2.4}$$

and,

$$\begin{aligned} S_i^\alpha S_j^\beta + S_i^\beta S_j^\alpha = & \frac{2}{3}\left(1 - \frac{1}{2}|\boldsymbol{\sigma}_i|^2 - \frac{1}{2}|\boldsymbol{\sigma}_j|^2\right) \\ & - \frac{\sqrt{2}}{3}\left(\boldsymbol{\sigma}_i + \boldsymbol{\sigma}_j\right) \cdot \boldsymbol{t}^\gamma \\ & + \frac{2}{3}\left[\left(\boldsymbol{\sigma}_i \cdot \boldsymbol{t}^\alpha\right)\left(\boldsymbol{\sigma}_j \cdot \boldsymbol{t}^\beta\right) + \left(\boldsymbol{\sigma}_i \cdot \boldsymbol{t}^\beta\right)\left(\boldsymbol{\sigma}_j \cdot \boldsymbol{t}^\alpha\right)\right] \end{aligned} \tag{2.5}$$

The external field term is approximated as:

$$\boldsymbol{H} \cdot \sum_i \boldsymbol{S}_i = \sum_i \left(1 - \frac{1}{2}|\sigma_i|^2\right) \tag{2.6}$$

Now we expand the Hamiltonian of Γ model subjected to a magnetic field to the form in terms of the forms derived above:

$$\begin{aligned} \mathcal{H} = & \Gamma \sum_{<ij>_x} \left(S_i^y S_j^z + S_i^z S_j^y\right) \\ & + \Gamma \sum_{<ij>_y} \left(S_i^x S_j^z + S_i^z S_j^x\right) \\ & + \Gamma \sum_{<ij>_z} \left(S_i^x S_j^y + S_i^y S_j^x\right) \\ & - \boldsymbol{H} \cdot \sum_i \boldsymbol{S}_i \end{aligned} \tag{2.7}$$

where $\gamma = x, y$, and z denote the three distinct NN bonds of a honeycomb lattice. Insert these expressions into the Hamiltonian of Gamma model. Note

that the linear terms vanish in lattice summation.

$$\begin{aligned}\mathcal{H} &= (\Gamma - H)N - (\Gamma - H)\sum_i |\boldsymbol{\sigma}_i|^2 \\ &+ \frac{2}{3}\Gamma \sum_{<i,j>} \sum_{\gamma} \left[(\boldsymbol{\sigma}_i \cdot \boldsymbol{t}^{\alpha}) \left(\boldsymbol{\sigma}_j \cdot \boldsymbol{t}^{\beta}\right) + \left(\boldsymbol{\sigma}_i \cdot \boldsymbol{t}^{\beta}\right) (\boldsymbol{\sigma}_j \cdot \boldsymbol{t}^{\alpha}) \right]\end{aligned} \tag{2.8}$$

The summation of last term in x-bond:

$$\sum_{<ij>_x} \left[(\boldsymbol{\sigma}_i \cdot \boldsymbol{t}^{y}) (\boldsymbol{\sigma}_j \cdot \boldsymbol{t}^{z}) + (\boldsymbol{\sigma}_i \cdot \boldsymbol{t}^{z}) (\boldsymbol{\sigma}_j \cdot \boldsymbol{t}^{y}) \right] \tag{2.9}$$

$$= \sum_{<ij>_x} \left[(\boldsymbol{\sigma}_1(\boldsymbol{r}) \cdot \boldsymbol{t}^{z})(\boldsymbol{\sigma}_2(\boldsymbol{r} + \boldsymbol{d}_x) \cdot \boldsymbol{t}^{y}) + (\boldsymbol{\sigma}_1(\boldsymbol{r}) \cdot \boldsymbol{t}^{y})(\boldsymbol{\sigma}_2(\boldsymbol{r} + \boldsymbol{d}_x) \cdot \boldsymbol{t}^{z}) \right] \tag{2.10}$$

$$= \sum_{\boldsymbol{r}} \left[t_y^m t_z^n \sigma_1^m(\boldsymbol{r}) \sigma_2^n(\boldsymbol{r} + \boldsymbol{d}_x) + t_z^m t_y^n \sigma_1^m(\boldsymbol{r}) \sigma_2^n(\boldsymbol{r} + \boldsymbol{d}_x) \right] \tag{2.11}$$

where $m, n \in \{a, b\}$. The third term summation in equation (5) over x, y, z is

$$\sum_{\boldsymbol{r}} \sum_{\alpha=\{x,y,z\}} \left[t_\beta^m t_\gamma^n \sigma_1^m(\boldsymbol{r}) \sigma_2^n(\boldsymbol{r} + \boldsymbol{d}_\alpha) + t_\gamma^m t_\beta^n \sigma_1^m(\boldsymbol{r}) \sigma_2^n(\boldsymbol{r} + \boldsymbol{d}_\alpha) \right] \tag{2.12}$$

Here the spin deviations $\boldsymbol{\sigma}_i$ are treated as classical variables. We analyze the eigenmodes of the classical Hamiltonian. Insert the Fourier expression of $\boldsymbol{\sigma}_i = \frac{1}{\sqrt{N}} \sum_{\boldsymbol{k}} \boldsymbol{\sigma}_s(\boldsymbol{k}) e^{i\boldsymbol{k}\cdot\boldsymbol{r}_i}$ to diagonalize the Hamiltonian above, the Hamiltonian becomes:

$$\mathcal{H} = E_0 + \sum_{\boldsymbol{k}} S_{\boldsymbol{k}}^* \mathbb{H}_{\boldsymbol{k}} S_{\boldsymbol{k}} \tag{2.13}$$

where $E_0 = N\Gamma - NH$, where N is the number of unit cells, and $S_k =$

$(\sigma^a_{1k}, \sigma^b_{1k}, \sigma^a_{2k}, \sigma^b_{2k})$ and

$$\mathbb{H}_{\boldsymbol{k}} = \begin{pmatrix} \epsilon & 0 & g^{aa}_{\boldsymbol{k}} & g^{ab}_{\boldsymbol{k}} \\ 0 & \epsilon & g^{ab}_{\boldsymbol{k}} & g^{bb}_{\boldsymbol{k}} \\ g^{aa}_{-\boldsymbol{k}} & g^{ab}_{-\boldsymbol{k}} & \epsilon & 0 \\ g^{ab}_{-\boldsymbol{k}} & g^{bb}_{-\boldsymbol{k}} & 0 & \epsilon \end{pmatrix} \tag{2.14}$$

The matrix elements are

$$\epsilon = H - 2\Gamma \tag{2.15}$$

$$g^{mn}_{\boldsymbol{k}} = \frac{2}{3}\Gamma \sum_{\alpha} \left(t^m_\beta t^n_\gamma + t^m_\gamma t^n_\beta \right) e^{i\boldsymbol{k}\cdot\boldsymbol{d}_\alpha} \tag{2.16}$$

$$g^{aa}_{\boldsymbol{k}} = -\frac{2}{3}\Gamma \left(e^{i\boldsymbol{k}\cdot\boldsymbol{d}_x} + e^{i\boldsymbol{k}\cdot\boldsymbol{d}_y} - \frac{1}{2} e^{i\boldsymbol{k}\cdot\boldsymbol{d}_z} \right) \tag{2.17}$$

$$g^{bb}_{\boldsymbol{k}} = -\Gamma e^{i\boldsymbol{k}\cdot\boldsymbol{d}_z} \tag{2.18}$$

$$g^{ab}_{\boldsymbol{k}} = g^{ba}_{\boldsymbol{k}} = \frac{1}{\sqrt{3}}\Gamma \left(-e^{i\boldsymbol{k}\cdot\boldsymbol{d}_x} + e^{i\boldsymbol{k}\cdot\boldsymbol{d}_y} \right) \tag{2.19}$$

where the three vectors $\boldsymbol{d}_x = (\frac{1}{2}, -\frac{1}{2\sqrt{3}})$, $\boldsymbol{d}_y = (-\frac{1}{2}, -\frac{1}{2\sqrt{3}})$ and $\boldsymbol{d}_z = (0, \frac{1}{\sqrt{3}}))$ play the functions of connecting nearest neighbors in honeycomb lattice. As is shown in figure , the magnetic instability starts at the $\boldsymbol{k}^8$ points when the external field decreases, and $\lambda_{\min(\boldsymbol{k})}$ has minima at K points. This suggests that the magnetic instability grows at the corners of the Brillouin zone.

Hamiltonian is η-invariant. At high magnetic field, spins in zigzag order will change into $\sqrt{3} \times \sqrt{3}$ order through a first-order transition until they are fully polarized by the external field. The lowest eigen-mode energy shown in Fig. 2.2 exhibits six minima at the corners of the Brillouin zone (BZ),

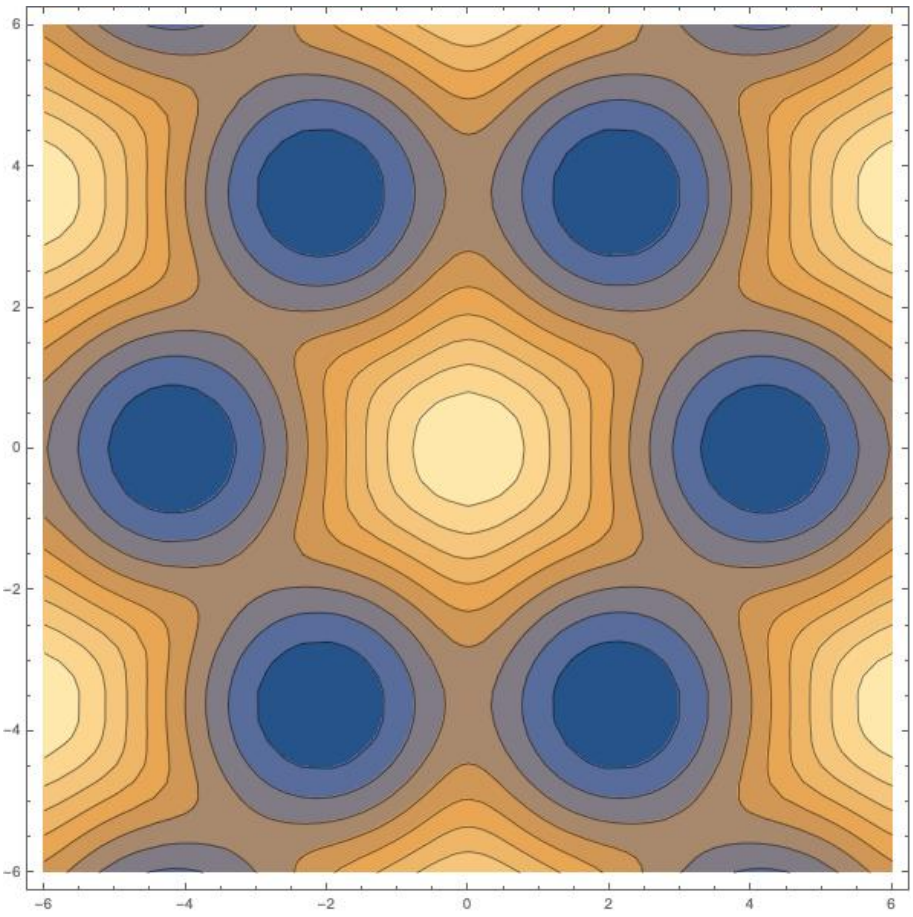

Figure 2.2: Contour plot of minimum eigenvalue of H_k, showing minimum at K points $Q_K = \left(\frac{4\pi}{3a}, 0\right)$

indicating that the most unstable mode has a wave vector $\boldsymbol{k}^* = (\frac{4\pi}{3a}, 0)$, where a is the lattice constant of the honeycomb lattice. This ordering wave vector corresponds to the $\sqrt{3} \times \sqrt{3}$ periodic structure in real space. Consequently, as the magnetic field is lowered below some critical value, the polarized state becomes unstable against the development of the $\sqrt{3} \times \sqrt{3}$ magnetic order. From the analytical solution of the minimum mode energy at the K-point, $\varepsilon_{\boldsymbol{k}^*} = H - 4\Gamma$, the instability condition $\varepsilon_{\boldsymbol{k}^*} = 0$ gives an upper critical field $H_{c2} = 4\Gamma$.

This conclusion is verified by our classical Monte Carlo simulations, for example, the magnetization curve at a low temperature $T = 0.01\Gamma$ ($|\Gamma|$ is set to 1 in the simulation), shown in Fig. 2.1 (b). At small magnetic field, the plaquette-ordered spin liquid remains stable up to some critical field H_{c1}, above which the flux order parameter $\Phi_{\sqrt{3}\times\sqrt{3}}$ drops abruptly. The magnetization M increases linearly in this intermediate regime until spins are fully polarized at $H \gtrsim H_{c2} = 4\Gamma$. Fig. 2.1(c) shows the static structure factor of the intermediate state, which exhibits six peaks at the corners of the BZ in addition to the central peak at $\boldsymbol{k} = 0$ due to the field-induced finite magnetization.

2.3 Ground State Configuration

We next determine the structure of the $\sqrt{3} \times \sqrt{3}$ state. The six inequivalent spins in the extended unit cell form an 18-dimensional representation of the little group of the K-point. The relevant magnetic order parameters, which can be obtained by examining the irreducible representations, can be very

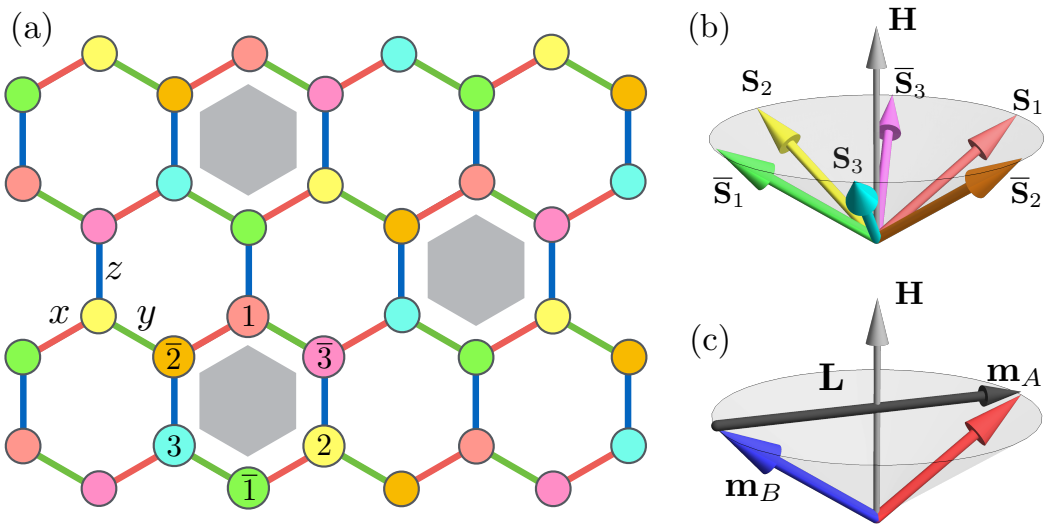

Figure 2.3: (a) The magnetic ground state of antiferromagnetic Γ-model in a [111] field. (b) Relative orientation of the six sublattice spins in the $\sqrt{3} \times \sqrt{3}$ magnetic order shown in panel (a). The complex spin structure can be described by two sublattice order parameter $\mathbf{m}_A$ and $\mathbf{m}_B$ shown in panel (c).

complicated. Our direct energy minimization, however, finds a rather simple magnetic structure which can be described by a Néel order parameter. Generalizing parametrization of spins in the special $\sqrt{3} \times \sqrt{3}$ ground state of the zero-field Γ-model [36], we introduce two sublattice order parameters $\mathbf{m}_A = (a, b, c)$ and $\mathbf{m}_B = (\overline{a}, \overline{b}, \overline{c})$. The six sublattice spins of the tripled unit cell, as labeled in Fig. 2.3, can be expressed as

$$\begin{aligned} \mathbf{S}_1 &= S(a, b, c), \quad \mathbf{S}_2 = S(b, c, a), \quad \mathbf{S}_3 = S(c, a, b), \\ \overline{\mathbf{S}}_1 &= S(\overline{b}, \overline{a}, \overline{c}), \quad \overline{\mathbf{S}}_2 = S(\overline{a}, \overline{c}, \overline{b}), \quad \overline{\mathbf{S}}_3 = S(\overline{c}, \overline{b}, \overline{a}). \end{aligned} \tag{2.20}$$

Remarkably, with this parametrization the energy of the complex $\sqrt{3} \times \sqrt{3}$ order is given by

$$E/N = \Gamma S^2 \mathbf{m}_A \cdot \mathbf{m}_B - \frac{1}{2} HS\hat{\mathbf{n}} \cdot (\mathbf{m}_A + \mathbf{m}_B), \tag{2.21}$$

which is exactly the same as the energy of the spin-flop state of a bipartite antiferromagnet [61, 62, 63]. To obtain the ground state, we introduce the magnetization vector $\mathbf{M}$ and a "Néel" vector $\mathbf{L}$ that characterizes the disparity of the two sublattices:

$$\mathbf{M} = (\mathbf{m}_A + \mathbf{m}_B)/2, \qquad \mathbf{L} = (\mathbf{m}_A - \mathbf{m}_B)/2. \tag{2.22}$$

In the classical ground state, these two order parameters satisfy the conditions: $\mathbf{M}^2 + \mathbf{L}^2 = 1$, and $\mathbf{M} \cdot \mathbf{L} = 0$. The energy in Eq. (2.21) is minimized when $\mathbf{M}$ and $\mathbf{L}$ are parallel and perpendicular to the field direction, respectively. The magnetization of the minimum-energy solution is $M = H/4S\Gamma$. The upper critical field obtained from the condition $M = 1$ of fully polarized spins is $H_{c2} = 4\Gamma S$, consistent with that derived from the stability analysis.

In terms of the order parameters, the energy per spin, $E/N = \Gamma S^2(\mathbf{M}^2 - \mathbf{L}^2) - HS\hat{\mathbf{n}} \cdot \mathbf{M}$, is invariant under rotation of the Néel vector around the field direction. As the Γ model itself does not possess such rotation symmetry, this accidental O(2) degeneracy is expected to be lifted when quantum or thermal fluctuations are taken into account. We first consider the quantum order-by-disorder mechanism and outline the linear spinwave calculation for the spin-flop state shown in Fig. 2.3(b). To this end, we write the Néel vector as

$\mathbf{L} = L(\cos\Theta\,\hat{\mathbf{e}}_1 + \sin\Theta\,\hat{\mathbf{e}}_2)$, where $L = \sqrt{1-M^2}$, and $\hat{\mathbf{e}}_{1,2}$ are two unit vectors perpendicular to the field direction introduced above; see Fig. 2.4(a). In the ground state, the six sublattice spins defined in Eq. (2.20) can be expressed as $\mathbf{S}_r = S\hat{\boldsymbol{\eta}}^z_{+,r}$ and $\overline{\mathbf{S}}_r = S\hat{\boldsymbol{\eta}}^z_{-,r}$ $(r = 1, 2, 3)$, where the quantization axes are

$$\hat{\boldsymbol{\eta}}^z_{\pm,r} = \pm L\left[\cos\left(\Theta + \omega_r\right)\hat{\mathbf{e}}_1 + \sin\left(\Theta + \omega_r\right)\hat{\mathbf{e}}_2\right] + M\hat{\mathbf{n}}.$$

Here $\pm$ corresponds to A/B sublattice, respectively, and $\omega_r = 0, \frac{2\pi}{3}, \frac{4\pi}{3}$ for $r = 1, 2, 3$, respectively. One can introduce an orthogonal triad of unit vectors for each sublattice by defining $\hat{\boldsymbol{\eta}}^x_{\pm,r} = \mp[\sin(\Theta + \omega_r)\hat{\mathbf{e}}_1 - \cos(\Theta + \omega_r)\hat{\mathbf{e}}_2]$ and $\hat{\boldsymbol{\eta}}^y_{\pm,r} = \hat{\boldsymbol{\eta}}^z_{\pm,r} \times \hat{\boldsymbol{\eta}}^x_{\pm,r}$. For convenience, we use $K_i = (s_i, r_i)$, where $s_i = \pm 1$ and $r_i = 1, 2, 3$, to denote the magnetic sublattice of site-i. Using the Holstein-Primakoff transformation, we write the spin operator at site-i as $\hat{\mathbf{S}}_i \approx \sqrt{2S}\left(\hat{a}^x_i\hat{\boldsymbol{\eta}}^x_{K_i} + \hat{a}^y_i\hat{\boldsymbol{\eta}}^y_{K_i}\right) + (S - \hat{a}^\dagger_i\hat{a}_i)\hat{\boldsymbol{\eta}}^z_{K_i}$, where $\hat{a}^x_i = (\hat{a}_i + \hat{a}^\dagger)/2$, $\hat{a}^y_i = (\hat{a}_i - \hat{a}^\dagger_i)/2i$, and $\hat{a}^\dagger_i$ $(\hat{a}_i)$ are the on-site magnon creation (annihilation) operators. Substituting the $\hat{\mathbf{S}}_i$ operator into Eq. (2.1), we obtain the following magnon Hamiltonian

$$\hat{\mathcal{H}} = E_{\rm SF} + 2\Gamma S\sum_i \hat{a}^\dagger_i\hat{a}_i + \sum_{\langle ij\rangle}\sum_{\mu\nu}^{x,y}\hat{a}^\mu_i\mathcal{M}^{\mu\nu}_{ij}\hat{a}^\nu_j, \tag{2.23}$$

where $E_{\rm SF} = -N(\Gamma S^2 + H^2/8\Gamma)$ is the energy of the spin-flop state, the coefficient $\mathcal{M}^{\mu\nu}_{ij} = 2S\hat{\boldsymbol{\eta}}^\mu_{K_i}\cdot\boldsymbol{\Gamma}_{ij}\cdot\hat{\boldsymbol{\eta}}^\nu_{K_j}$, and $\boldsymbol{\Gamma}_{ij}$ is the Gamma-interaction matrix on $\langle ij\rangle$ bond.

The magnon Hamiltonian is then diagonalized using Fourier and Bogoliubov transformations. Figs. 2.4(c) and (d) show the spinwave spectrum $\omega_n(\boldsymbol{k})$,

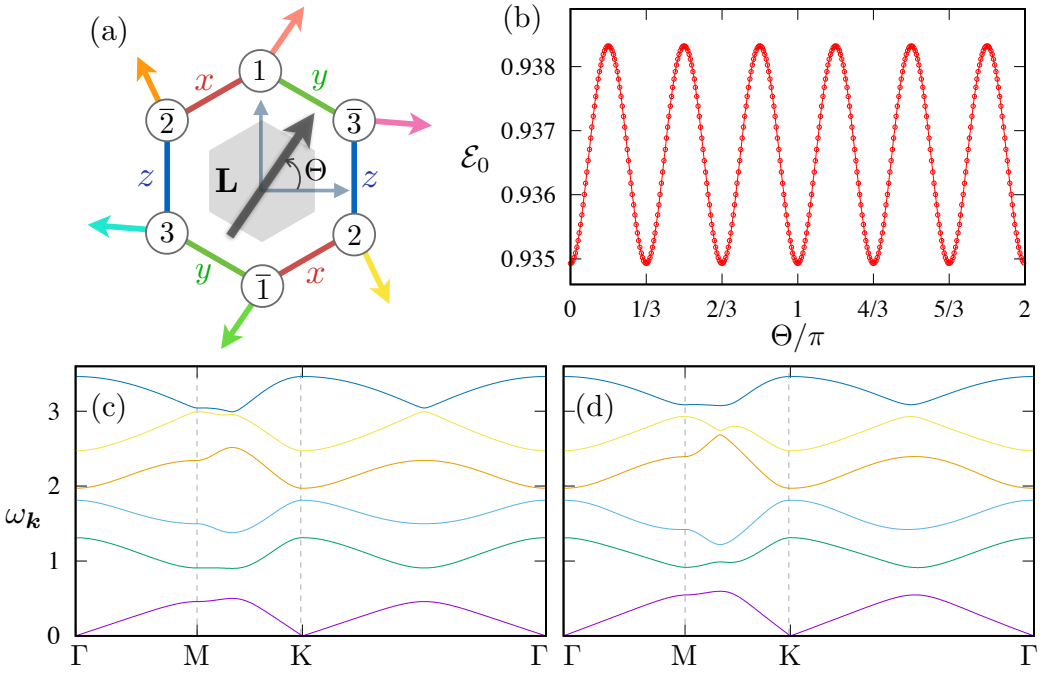

Figure 2.4: (a) Néel vector $\mathbf{L} = L(\cos\Theta\,\hat{\mathbf{e}}_1 + \sin\Theta\,\hat{\mathbf{e}}_2)$ associated with a hexoagon; here $\hat{\mathbf{e}}_1 = (\hat{\mathbf{e}}_x + \hat{\mathbf{e}}_y - 2\hat{\mathbf{e}}_z)/\sqrt{6}$ and $\hat{\mathbf{e}}_2 = (\hat{\mathbf{e}}_x - \hat{\mathbf{e}}_y)/\sqrt{2}$ are two unit vectors perpendicular to the [111] field direction. (b) Zero point energy of magnons as a function of angle Θ for magnetization $M = 0.5$. The spinwave spectra at $\Theta = 0$ and $\pi/6$ are shown in panels (c) and (d), respectively.

where $n = 1, \cdots, 6$ is the band index, along high-symmetry directions of the BZ for two different angles $\Theta = 0$ and $\Theta = \pi/6$, respectively. In both cases, a pseudo-Goldstone mode [64] is obtained at the center and corners of the BZ, which can be attributed to the O(2) symmetry combined with a Z_3 symmetry associated with the $\sqrt{3} \times \sqrt{3}$ order. The different spectra also means that the quantum zero-point energy, given by the sum $\mathcal{E}_0 = \sum_{n,\boldsymbol{k}} \omega_n(\boldsymbol{k})/2$, depends on the orientation angle Θ of Néel vector. As shown in Fig. 2.4(b), the zero-point energy exhibits six minima at $\Theta = m\pi/3$, where m is an integer, indicating that these six orientations, related by the hexagonal symmetry of the Γ-model, are favored by quantum fluctuations.

2.4 Order by Disorder

At non-zero but low temperatures the accidental O(2) degeneracy is also lifted by thermal order by disorder, which selects the same six-fold degenerate ground state, as confirmed by our Monte Carlo simulations. However, the O(2) symmetry is restored at further elevated temperatures and persists within a finite window, giving rise to a critical XY phase. Indeed, field-induced XY criticality in the spin-flop state of 2D bipartite antiferromagnets has been reported for both classical and quantum spins [65, 66, 67, 68, 69, 70, 71]. As the Néel order in the spin-flop state is forced to lie in a plane perpendicular to the field direction, the magnet effectively becomes an XY system.

For the Gamma model, a local Néel vector can be defined for each hexagon, for example $L^x = S_1^x - \overline{S}_1^y + S_2^z - \overline{S}_2^x + S_3^y - \overline{S}_3^z$, and so on for the y and z

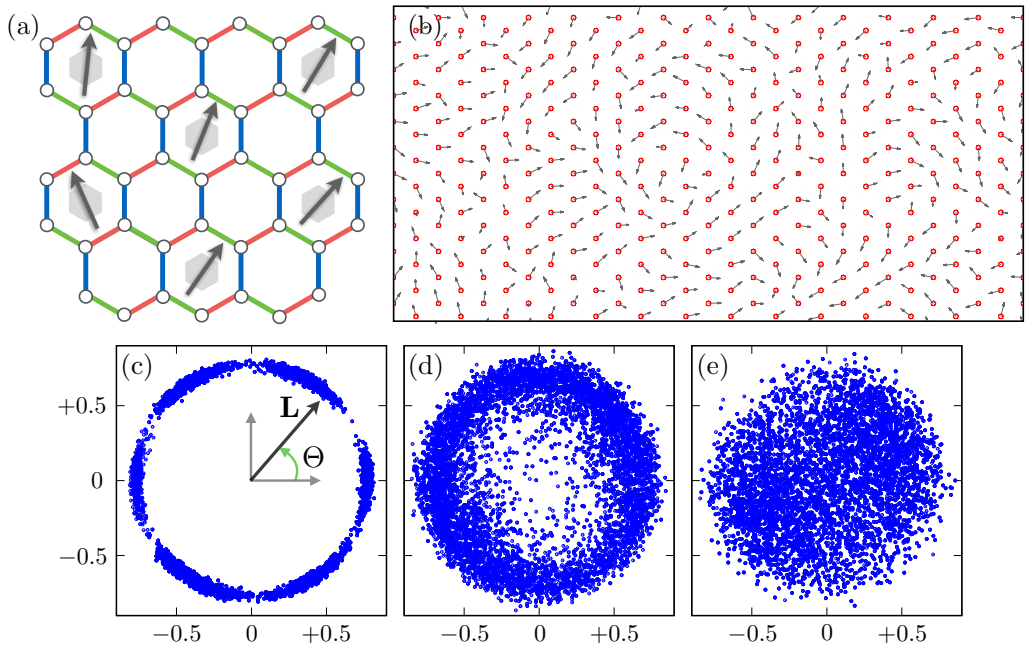

Figure 2.5: (a) Schematic diagram showing ordering of local Néel vectors $\mathbf{L}_\alpha \sim (\cos\Theta_\alpha, \sin\Theta_\alpha)$ associated with shaded hexagons representing a local magnetic unit cell. (b) A snapshot of $\mathbf{L}$-vector at $H = 2\Gamma$ and $T = 0.1\Gamma$. The histogram of the $\mathbf{L}$ vectors at temperatures (c) $T = 0.01\Gamma$, (d) $T = 0.1\Gamma$, and (e) $T = 0.2\Gamma$.

components; see Eq. (2.20). These local Néel vectors behave as XY spins at low temperatures in the spin-flop state of the Γ model. A snapshot of the hexagonal $\mathbf{L}$-vectors at $T = 0.1\Gamma$ is shown in Fig. 2.5(b). Importantly, the low-temperature behaviors of the Gamma model can be described by a ferromagnetic XY model subject to a six-state clock anisotropy. The breaking of the Z_6 symmetry in this model is known to go through two Berezinskii-Kosterlitz-Thouless (BKT) transitions which enclose an intermediate critical XY phase [72, 73], a scenario that is confirmed in our Monte Carlo simulations. As demonstrated by the histogram of local Néel vectors at three different temperatures shown in Fig. 2.5(c)–(e), an O(2) rotational symmetry emerges in the

intermediate critical phase where the spin-spin correlation decays algebraically with distance.

2.5 Monte-Carlo Simulations and Phase Diagram

The various thermodynamic phases obtained from Monte Carlo simulations are summarized in the magnetic field H versus temperature T phase diagram shown in Fig. 2.6(a). Depending on strength of the magnetic field, the Γ model follows two different routes to reach the $\sqrt{3} \times \sqrt{3}$ magnetic order. While the high-field scenario is through two BKT transitions described above, at small magnetic fields, the system undergoes a crossover and two phase transitions to reach the $\sqrt{3} \times \sqrt{3}$ magnetic ground state. As temperature is lowered below the exchange energy scale, the magnet first enters a classical spin liquid regime with short-range correlation [35]. This is followed by another spin liquid with $\sqrt{3} \times \sqrt{3}$ ordering of plaquette fluxes through a continuous phase transition [36]. Upon further lowering the temperature, the plaquette spin liquid phase stabilized by its configurational entropy gives way to the energetically favored magnetic ground state via a first-order transition.

Despite both having the same wave vector, the ordering of hexagonal fluxes is incompatible with that of spins, which is why the transition between them is of first-order. It is also instructive to understand this discontinuous transition from the viewpoint of spin orientations. The ordering of the fluxes is accompanied by the alignment of spins toward the cubic x, y, z directions due

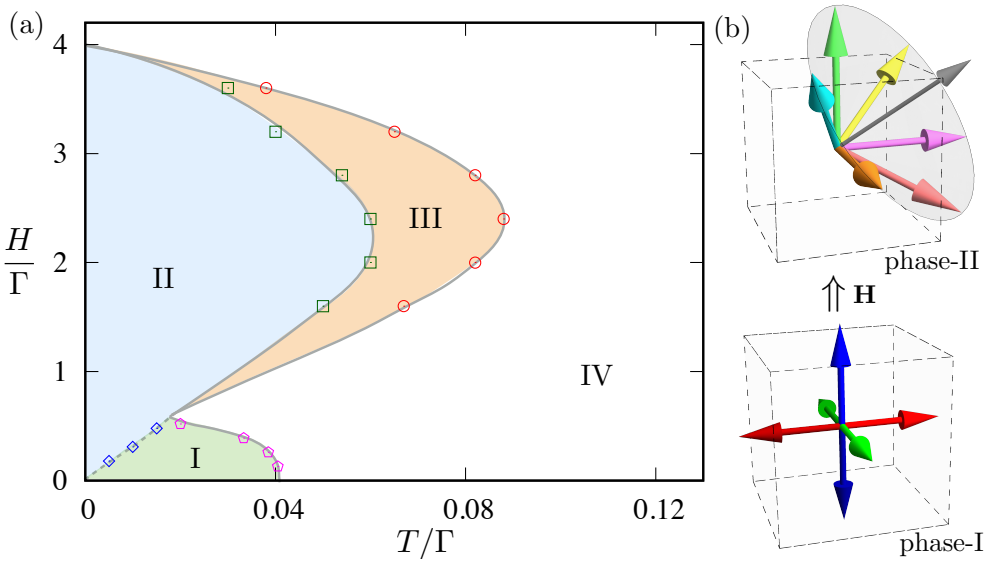

Figure 2.6: (a) Schematic phase diagram of the classical Γ model obtained from Monte Carlo simulations. The various phases are: (I) spin liquid with hexagonal flux order that breaks the lattice translation symmetry. (II) Long-range $\sqrt{3}\times\sqrt{3}$ magnetic order with a tripled unit cell. (III) Critical XY phase with an emergent O(2) symmetry of Néel vectors. (IV) Classical spin liquid with short-ranged correlation that is smoothly connected to high-T paramagnet and the polarized state at high field. (b) the transition from the plaquette spin liquid to the $\sqrt{3}\times\sqrt{3}$ magnetic order resembles a spin-flop transiton in bipartite antiferromagnet with weak anisotropy.

to order-by-disorder [35, 36]. Notably, the Néel order parameter can still be used to describe the "opposite" orientations of the two sublattices in the antiferromagnetic case, although *no* long-rang spin order develops because of the emergent Ising pseudo-gauge symmetry. The order-by-disorder mechanism at small fields thus effectively induces a cubic anisotropy for the Néel vector: $E_{\text{cubic}} = -D(L_x^4 + L_y^4 + L_z^4)$. The competition between this anisotropy and the zeeman coupling to magnetic field leads to a first-order transition similar to the well-studied spin-flop transition [61]; see Fig. 2.6(b).

To summarize, we have uncovered a novel field-induced magnetic ground

state in the antiferromagnetic honeycomb Gamma model. This complex magnetic order with a tripled unit cell is a spin-flop state in disguise, and can be described by a hidden Néel order parameter. Moreover, we show that the first-order transition between the low-field spin liquid with an effective cubic spin anisotropy and the high-field magnetic order resembles the spin-flop transition in a bipartite antiferromagnet. Although our semiclassical analysis only applies to large-spin Gamma model, it is likely that this magnetic order is stabilized at high magnetic field even for quantum spin-1/2. A related intriguing question is what happens to the ground state of spin-1/2 Gamma model, which seems to be a gapless spin liquid that is proximate to a zigzag order [74, 75], in the presence of magnetic field. Also of interest is the effect of other exchange interactions on the spin-flop state of the Γ model reported here. Our work sheds a new light on the nature of complex magnetic structures in such frustrated spin-orbit systems.

Chapter 3

Numerical Study of Double Perovskite $\mathbf{Sr_2CuTe_{1-x}W_xO_6}$

The states of many types of frustrated magnetism models still form a magnetic long-range order when the temperature reaches even much lower than Θ_{CW}. However, there is a type of frustrated magnets that behaves randomly, such that their spins stay dynamical at zero temperature. One of these intriguing frustrated magnets is the quantum spin liquid (QSL). QSLs do not develop any long range order at any temperature in any local order parameter. They are highly entangled states that exhibit many unique features involving their topological characteristics. One of these characteristics is that elementary excitations of the state are like fractions of an electron[76]. These exotic properties of QSLs enable a possible application of topological computing. Since it was proposed theoretically by Anderson, there has been many experimental efforts focusing on geometrically frustrated magnets, in the expectation that

the induced competing interactions can lead to the spin liquid state.

However, several studies indicate that for some promising QSL candidates, such as $NiGa_2S_4$, α-$RuCl_3$, their spins will undergo a transition such that they will freeze when temperature descends to a certain point. Such a transition is called a glass transition. The 'freezing' temperature is defined as T_f. Akin to spin liquids, directions of spins in spin glasses remain random in very low temperature even though they do not rotate anymore.

The spin glass concept was first introduced to describe diluted magnetic alloys, such as AuFe and AgMn, in which nonmagnetic metal is diluted by magnetic impurities. When ions of magnetic metal (such as Mn, Fe) are mixed into nonmagnetic noble metals (such as Au, Cu, Pt) in small doses, the impurity spins inside the alloy interact through a mechanism called Ruderman-Kittle-Kasuya-Yosida (RKKY) exchange. The RKKY theory introduces an indirect exchange coupling in which conduction electrons create a correlation energy between two nuclear spins by interacting with the nuclear spins through hyperfine interactions [77, 78, 79]. The corresponding Hamiltonian is written as:

$$\begin{aligned} H(\mathbf{R}_{ij}) =& \frac{\mathbf{I}_i \cdot \mathbf{I}_j}{4} \frac{|\Delta_{k_m k_m}|^2 m^*}{(2\pi)^3 R_{ij}^4 \hbar^2} \\ & \cdot [2k_m R_{ij} \cos(2k_m R_{ij}) - \sin(2k_m R_{ij})], \end{aligned}$$

where R_{ij} is the distance between ions of impurities I_i is the nuclear spin of atom i, m^* is the effective mass of electrons, and $\Delta_{k_m k_m}$ are the elements in a matrix which represents the strength of the hyperfine interaction. This dis-

tance term can determine the sign and magnitude of the RKKY interactions, resulting in a competition between ferromagnetic and antiferromagnetic interactions inside the alloy. Combining with spatial disorder, the mechanism provides conditions for forming a spin glass state.

Later, Edwards and Anderson came up with a model to extend the concept of spin glass to regular lattice systems [80]. Their model assumes that spin interactions are short-ranged and, that their signs are randomly assigned. In the model, the Hamiltonian between two spins is formulated as $H_{ij} = J_{ij} S_i \cdot S_j$, where J_{ij} is a randomly assigned number for interaction. Since then, extensive numerical simulations based on this model have been undertaken in order to investigate the presence of a finite-temperature glass transition for Heisenberg-like spins, and exponents in the corresponding universality class are well extracted [81].

3.1 J_1-J_2 Antiferromagnetic System

We have discussed the basic concepts of the J_1-J_2 system in the introduction. But before we move on to the details of the disordered J_1-J_2 system, the J_1-J_2 model needs to be discussed in detail first.

The J_1-J_2 Heisenberg model is a simple magnetic system that can well demonstrate many 2D frustrated magnet phenomena, such as classical degeneracy, order by disorder, and so on. The model can particularly help us to understand the competing interactions in frustrated magnetism as well as the origin of the spin liquid in 2D lattice systems. Here we start our discussion

with the classical ground state of a translation invariant Heisenberg model on a square lattice. The model is defined as the following equation:

$$\mathcal{H} = -J_1 \sum_{<ij>} \mathbf{S}_i \cdot \mathbf{S}_j - J_2 \sum_{<<ij>>} \mathbf{S}_i \cdot \mathbf{S}_j, \tag{3.1}$$

where J_1 is the nearest neighbor interaction and J_2 is the next nearest neighbor interaction (through the diagonal of the square). Usually the classical ground states of such a translation invariant Heisenberg model on a Bravais lattice can be found by minimizing system energy by alternating expressions of a planar helix as $\vec{S}(\mathbf{r}) = \vec{e}_1 \cos(\mathbf{q} \cdot \mathbf{r}) + \vec{e}_2 \sin(\mathbf{q} \cdot \mathbf{r})$ into the model, such that the pitch $\mathbf{q}$ would minimize the model's Fourier transform $J(\mathbf{q})$:

$$\begin{aligned} J(\mathbf{q}) =& J_1(\cos(q_x) + \cos(q_y)) \\ &+ J_2(\cos(q_x + q_y) + \cos(q_x - q_y)). \end{aligned}$$

Alternating the ratio of J_1/J_2 shows there are two ground states for the classical J_1-J_2 Heisenberg model: Néel antiferromagnetic order (NAF), and columnar antiferromagnetic order (CAF). The difference in microscopic view can be explained as following: when $J_2 < 0.5J_1$, $J(\mathbf{q})$ has a single minimum at (π, π) corresponding to NAF; when $J_2 > 0.5J_1$, the $J(\mathbf{q})$ has two minima appearing in $(\pi, 0)$ and $(0, \pi)$ respectively. As for the case $J_2 \simeq 0.5J_1$, the ground state is highly degenerate. $J(\mathbf{q})$ would have lines of minima around the edges of the Brillouin zone. The zero-temperature quantum corrections to the sublattice magnetization have great divergence at this point. The approximation of large S usually overestimates the stability of magnetic phases, hence breaking

down at the point is a strong evidence suggesting the existence of quantum disordered phases [82]. The disordered J_1-J_2 Heisenberg model does not have fixed J terms. Instead, the values of nearest neighbor interactions and next nearest neighbor interactions are determined by the specific neighboring spin pairs. Several studies indicated that disorder in frustrated magnetism could lead QSLs into spin glass states [83, 84, 85]. The next step for us to investigate the glass transition in a disordered J_1-J_2 system.

3.2 Double Pervovskite Compound $SrCuTe_{1-x}W_xO_6$

The double perovskite compounds $SrCuTe_{1-x}W_xO_6$ provides an excellent stage for researching the disordered J_1-J_2 Heisenberg model, and it is also a possible candidate for quantum spin liquids. In this compound, Cu ions are separated by nonmagnetic Te and W cations in B-site ordered AB'B"O compounds $SrCuTeO_6$ and $SrCuWO_6$ respectively, and the magnetic coupling is a result of the superexchange mechanism. The compound can be modeled to a nearly ideal square lattice disordered J_1-J_2 system. Therein, the Cu cations can be modeled on a 2-dimensional square lattice in the xy plane, while diamagnetic B" cations dominate the superexchange pathways between Cu cations. By manipulating the ratio of numbers of Te and W ions in the system, one can alter the ratio of nearest neighbor J_1 and next nearest neighbor J_2 exchange interactions. Thereby the system can show various behaviors including of Neel antiferromagnetism, frustrated magnetism and columnar antiferromagnetism. B" cations Te and W ions are randomly distributed in the compound, result-

ing in a disorder in magnetic coupling that suppresses the magnetic order. When the tungsten ratio x in the range $|0.1 \sim 0.7|$, the system will behave like frustrated magnets. When the ratio J_2/J_1 reaches around $0.4 \sim 0.5$, magnetic frustration is expected to be maximized and a QSL ground state may emerge in the system.

It is rather difficult to find the freezing temperature for most of spin glass candidates, since T_f is usually very small. Similarly, earlier experimental researches on $SrCuTe_{0.5}W_{0.5}O_6$ did not observe any evidence for the existence of freezing temperature. The compound exhibits strong antiferromagnetic interactions and a corresponding Θ_{CW} is found at -71K. A neutron scattering study show a spin-wave like dispersion exhibited by the dynamics spin correlations in the QSL phase [86]. Moreover, a μSR study found that the spin correlations in this system remains entirely dynamical at temperatures as low as 19 mK [87]. However, a recent study presented the evidence of the freezing temperature, and a discovered Goldstone-like modes at very low temperatures [88].

Since the existence of glass transition in the compound $SrCuTe_{0.5}W_{0.5}O_6$ has now been confirmed, and since these exotic forms of complex order break SU(2) symmetry and support Goldstone modes, we can investigate the phenomena by semi-classical (spin-wave-like) numerical approximations.

In this study, we shall first present a study based on a series of Monte-Carlo simulations in order to search for glass transitions in the disordered J_1-J_2 system on a 2-dimensional square lattice. Then we shall present a numerical Landau-Lifschitz dynamics study for the system showing that a long

range spin-wave dispersion that survives the incoherent excitation even in the frustrated region of disordered J_1-J_2 system.

3.3 Monte Carlo Simulations

Conventionally, the disordered J_1-J_2 Heisenberg model is described by the Hamiltonian:

$$\mathcal{H} = -\sum_{\text{NN}} J_{ij}^{(1)} S_i S_j - \sum_{\text{NNN}} J_{ij}^{(2)} S_i S_j \tag{3.2}$$

where each NN exchange coupling $J_{ij}^{(1)}$ randomly distributes in $[J_1 - \Delta^{(1)}, J_1 + \Delta^{(1)}]$, and each NNN exchange coupling $J_{ij}^{(2)}$ randomly distributes in $[J_2 - \Delta^{(2)}, J_2 + \Delta^{(2)}]$ with constant Δs. The commonly used distribution for J values is a Gaussian distribution: $P_{ij} = \frac{1}{\sqrt{2\pi J^2}} \exp\left(-J_{ij}^2/2J^2\right)$, where J is the variance and the mean is zero. The energy scale is chosen to suffice $|J_{ij}|^2_{avg} = 1$.

However, the material $Sr_2CuTe_{1-x}W_xO_6$ gives us a realistic way to construct the disordered J_1-J_2 system. In the specific J_1-J_2 system for the compound, the values of a specific exchange J_1 and J_2 between two spins randomly distribute in the system such that $J_{ij}^{(1)} \in \{J_a, J_b, J_c\}$ and $J_{ij}^{(2)} \in \{J_d, J_e\}$. Since the value for interaction in the vertical direction J_z is considered to be too small to impose serious influence on elements in the square lattice defined on the xy plane, the compound can be treated as an effective 2-dimensional square lattice model. In this study we assume Te and W atoms are perfectly ordered such that each Cu^{2+} cation is surrounded to two Te^{6+} and two W^{6+} ions. As is shown in figure 3.1, there are three types of NN (J_a, J_b, and J_c) and two types of NNN (J_d and J_e) exchange couplings. Since the exchange coupling between

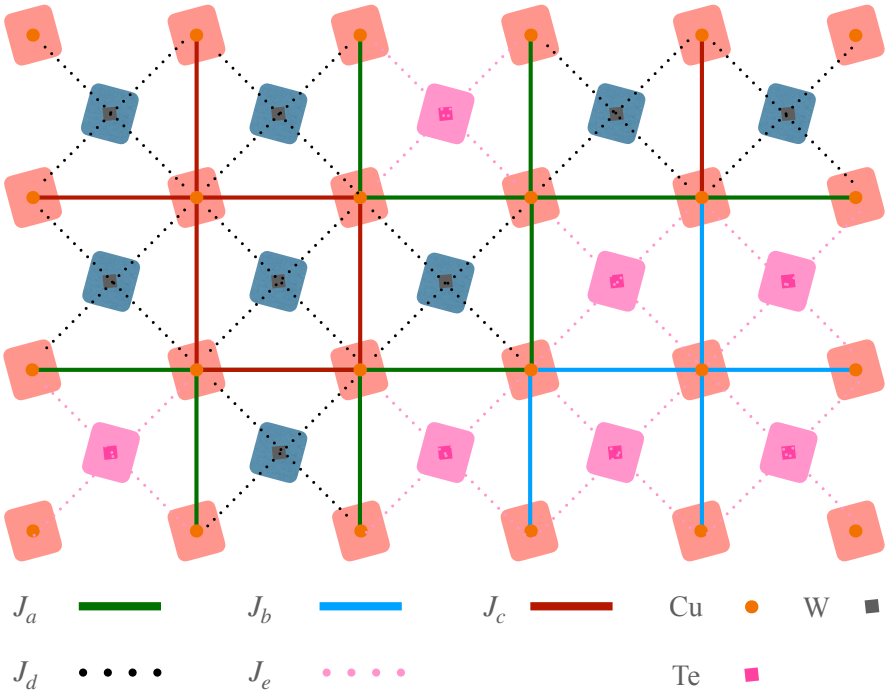

Figure 3.1: Spin-1/2 square lattice disordered J_1-J_2 scheme and NN and NNN exchange interactions in $Sr_2CuTe_{1-x}W_xO_6$. In the periodic lattice setting, tungsten and tellurium ions are randomly distributed in the system by the constant probability x. J_1 type disordered bonds are determined by two neighboring W and/or Te ions. J_2 type disordered bonds are determined by the W or Te ion in between.

Exchange couplings		
	QC	INS
J_a	0.	0.
J_b	7.38	7.6
J_c	0.68	1.02
J_d	8.33	8.5
J_e	0.05	0.6

Table 3.1: Heisenberg exchange couplings obtained from ab-initio MR-DDCI calculations (QC) and inelastic neutron scattering (INS) experiments for Sr_2CuTeO_6 and Sr_2CuWO_6 . All values are given in meV.

Cu cations is only determined by the binary choice of its corner element (Te or W), we can simplify the model to a lattice of Cu cations with its upright corner element (Te or W). To simulate the random distribution of tungsten atoms in the compound, we designed a function to randomly assign the upright corner element of each Cu ion in the system with the probability corresponding to the tungsten/tellurium ratio. For example, for $Sr_2CuTe_{0.7}W_{0.3}O_6$, there is a 30% probability the atom will be tungsten. Thus the proportion of tungsten atoms in the systems might not be exactly 30%. Then we can set the disorder bonds between Cu spins by its corner element and corner element of the nearest neighbor. After the disorder bonds are set in the program, a standard Metropolis-Hasting algorithm based on local updates is used to sample spin configurations once the thermal equilibrium is reached.

The values of Heisenberg exchange couplings J_a, J_b, J_c, J_d and J_e used for Monte-Carlo simulations in this study are acquired from ab-initio MR-DDCI calculations (QC) and inelastic neutron scattering (INS) experiments for Sr_2CuTeO_6 and Sr_2CuWO_6 [89, 90]. Their values are shown in the table 3.1.

3.4 Glass Transition at Zero Temperature

According to Edwards and Anderson [80], if spin glass transition exists, there would exist a type of orientations of the spins that yields the minimum of potential energy, and the type of orientations suffice $< S_i >= 0$ such that the system is neither in ferromagnetic nor in antiferromagnetic states. Also the system does not need to be unique. The central point of the argument is that if two observations are made for one particular spin S_i with a long time period in between, there exists a non-vanishing probability such that two spins are pointing in the same direction: $q =< S_i^{(1)} \cdot S_j^{(2)} >\neq 0$.

The spin glass transition, when there is no external field and when it is approached from a relatively high temperature, can be signalized by a divergence of the spin glass susceptibility, which is defined by:

$$\chi_{SG}(\mathbf{k}) = \frac{1}{N}[\sum_{i,j}\langle \mathbf{S}_i\mathbf{S}_j\rangle_T^2]_{\text{average}} \tag{3.3}$$

where the items in $\langle \quad \rangle_T$ denotes a thermal average and $[\quad]_{average}$ denotes the average over different disordered runs. In an infinite system, the susceptibility is supposed to follow the following relation:

$$\chi_{SG}(\mathbf{k}) \sim (T - T_C)^{-\gamma}, \tag{3.4}$$

where T_C is the transition temperature and $\gamma = (2 - \eta)\nu$. ν and η suffice the universality class for Ising model, in which η denotes the power law decay of the correlation at T_C, and ν is the exponent of the spin glass correlation length

ξ for $T \gtrsim T_C$.

$$G_2(r_{ij}) := [< S_i S_j >_T^2]_{\text{average}} \sim \frac{f(r_{ij}/\xi)}{r_{ij}^{d-2+\eta}} \tag{3.5}$$

and ξ diverges by the relation:

$$\xi \sim (T - T_C)^{-\nu}. \tag{3.6}$$

Now rewrite the Edwards-Anderson spin-glass order parameter as:

$$q = [\langle S_i \rangle_{\mathrm{T}}^2]_{\text{average}} \sim (T_C - T)^{\beta}, \tag{3.7}$$

where $\beta = (d - 2 + \eta) \cdot \nu/2$ and d is the dimension of the system. Since for the 2D glass order transition, the transition temperature $T_C = 0$, there is only one independent static exponent ν we need to extract.

As for Monte-Carlo simulations, the thermal averages can be replaced by time averages from two identical disorder realizations of the system with the same set of interactions. The double replica technique can also accelerate the simulation [**bose19**]. Thus in our Monte-Carlo simulations, spin glass order parameters at the wave vector $\mathbf{k}$ are defined as:

$$q_{EA}^{\alpha\beta}(\mathbf{k}) = \frac{1}{N} \sum_{i=1}^{N} \mu_i^{\alpha(1)} \mu_i^{\beta(2)} \exp(i\mathbf{k} \cdot \mathbf{r}_i) \tag{3.8}$$

In the equation, $\alpha, \beta = x, y, z$ are the spin components and (1) and (2) denote two disorder simulations with identical settings. $\langle \cdots \rangle$ denotes thermal average

over elongated time and $[\cdots]$ denotes different disorder averages.

$$\chi_{SG}(\mathbf{k}) = N \sum_{\alpha,\beta} [\langle |q_{EA}^{\alpha\beta}| \rangle] \tag{3.9}$$

As is discussed earlier, χ_{SG} would diverge as the lattice size $L \to \infty$. Of particular interest to us is the $\chi_{SG} \equiv \chi_{SG}(\mathbf{k} = 0)$. Furthermore, the correlation length ξ is defined as follows:

$$\xi = \frac{1}{2 \sin \frac{\mathbf{k}_{\min}}{2}} \left(\frac{\chi(\mathbf{k} = 0)}{\chi(\mathbf{k}_{\min})} - 1 \right)^{1/2} \tag{3.10}$$

where $k_{\min} = \frac{2\pi}{L}(1, 0, 0)$. In the case that the glass transition should be continuous in real life, the ratio ξ/L is closer to a university value characteristic of the critical point when L approaches infinity.

It is important to make sure that the results obtained from MC simulation can describe equilibrium fluctuation correctly. Because spin dynamics are often accompanied by frustrations and disorders, the length of these simulations usually have logarithmic time dependence, thus it must be conducted over a prolonged time period. Not only that, result states are quenched in disorder, and therefore averaging a large number of independent samplings would be necessary in order to sample fluctuations, and thus, to get relatively accurate results.

In our simulations for finding the glass order, the tungsten ratio is set to 0.3, which falls in the frustrated magnetism areas of the disordered J_1-J_2 model. For ensuring the correctness of our results, at a given temperature, systems from 50 different disordered initial states were sampled and in each of

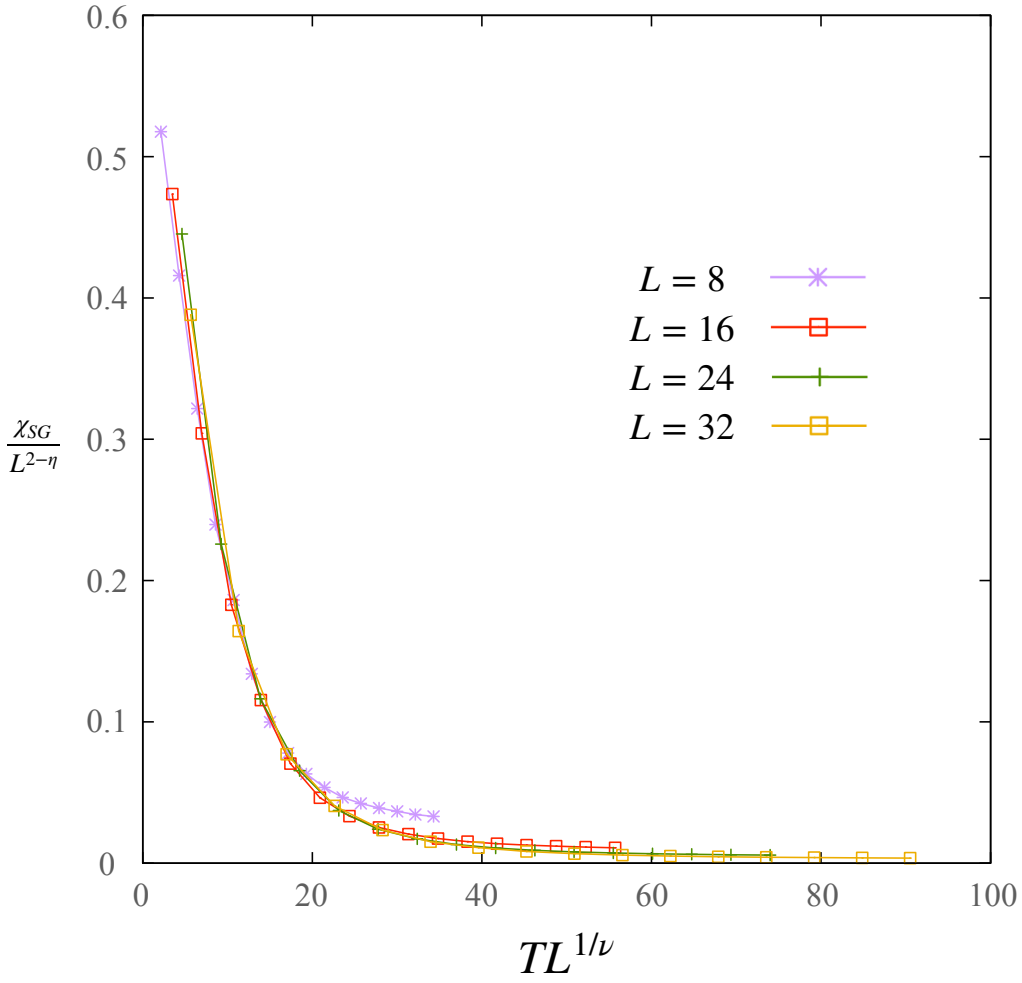

Figure 3.2: Finite size scaling plot of the spin glass susceptibility. The transition temperature is at $T_C = 0$.

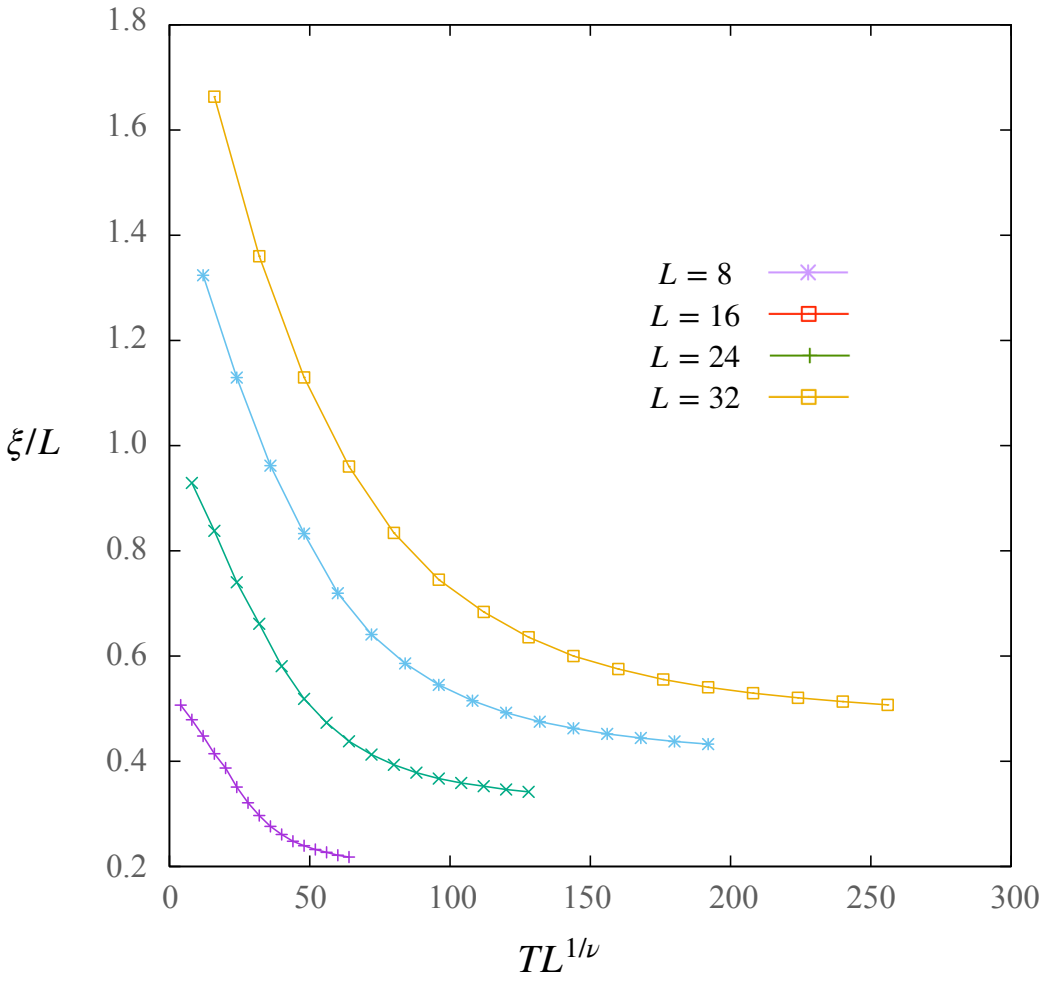

Figure 3.3: The dimensionless spin glass correlation length.

these systems, 5,000 samplings for thermal averaging were captured.

The algorithm in simulations mainly follows the Eq. 3.8 and Eq. 3.9. The result of the extensive Monte-Carlo simulation is shown in figure 3.2. It is noteworthy that the size dependence of χ_{SG} is as expected, namely that χ_{SG} gets larger as the system size L increases. Evidently when the temperature approaches to zero ($T_C = 0$), the χ_{SG} tends to approach infinity. The finite size scaling collapse of χ_{SG} gives us the value of $\nu_{SG} = 1.0 \pm 0.1$. In addition to it, we observe that correlation length also scales with ν_{SG}(fig. 3.3). The result agrees with the result of a previous study on 2D disordered Heisenberg model [91], which has the results $\nu_{SG} = 1.0 \pm 0.15$.

3.5 Landau Lifshitz Dynamics

The next step is to investigate the dynamical behaviors of the spin glass. In order to do it, we employ the semi-classical Landau-Lifshitz dynamics (LLD) technique [92]. In past decades, LLD has proved itself to be a very useful tool for studying the dynamic structure factor of various classical spin liquid systems. Here we are going to use LLD technique to investigate the disordered J_1-J_2 system as is exhibited in the compound $SrCuTe_{1-x}W_xO_6$.

In this study, we first conducted MC simulations to prepare initial states in thermal equilibrium for $T > T_f$, where T_f is T_C discussed in sec 3.4. Then, we use energy-conserving LLD equation to calculate trajectories of spins $\mathbf{S}_i(t)$ over time. Finally, we use real space correlator $\langle S_i^{\alpha}(t) S_j^{\beta}(0) \rangle$ to compute the dynamic structure factor $\mathcal{S}^{\alpha\beta}(\mathbf{k}, \omega)$, in which α, β are the space components

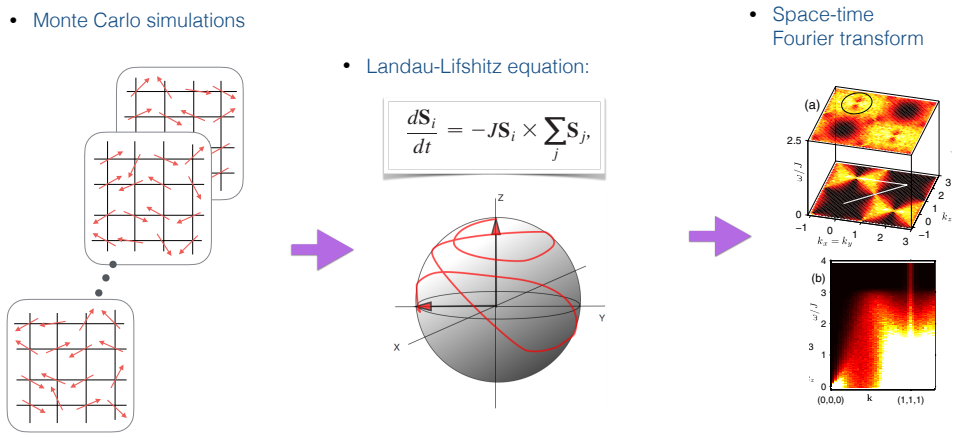

Figure 3.4: Numerical scheme of Landau-Lifshitz dynamics.

of the initial states.

The dynamics of the classical spins can be described by the LLD equation as is shown in follows:

$$\frac{d\mathbf{S}_i}{dt} = -\mathbf{S}_i \times \frac{\partial \mathcal{H}}{\partial \mathbf{S}_i} \tag{3.11}$$

where $\mathbf{B_i} = -\frac{\partial \mathcal{H}}{\partial \mathbf{S}_i}$ is the molecular field acting on the spin $\mathbf{S}_i$, and $\mathcal{H}$ is the Hamiltonian of the disordered J_1-J_2 system. Dissipation terms, like Gilbert damping, are not included in the equation since we focus on the un-damped oscillations of the excitations. Time-domain Fourier transform is employed to calculate the excitation energies from these oscillations. Here we use a half-explicit algorithm to realize the LLD equation in computer programs. The algorithm preserves the spin length at every time step and energy values remain conserved with time, independent of time length or size of time steps

in the simulation. In the simulation, we used square lattice sizes of $L = 90$ and $L = 120$. Time step is set to be $\Delta t = 0.001$ and total time length $T = 2000$ are used in setting.

Through MC simulations, we acquire the system states $\mathbf{S}_i^{eq}$ in thermal equilibrium. Then we use them as the initial spin configurations for the LL simulations. From these initial states, the program can compute the space-time Fourier transform:

$$\mathbf{S}(\mathbf{k}, \omega) = \frac{1}{N} \sum_i \int_0^T \mathbf{S}_i(t) e^{i\mathbf{k}\cdot\mathbf{r}_i} e^{-i\omega t} dt \tag{3.12}$$

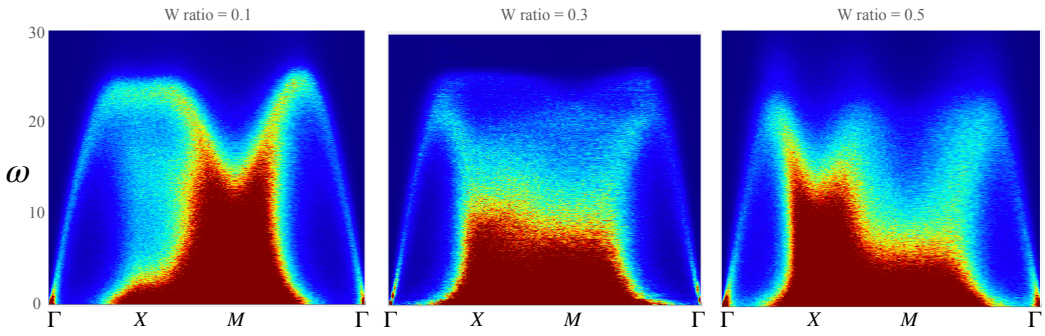

Figure 3.5: Dynamic structure factor against k values on the high symmetry path Γ-X-M-Γ. For the tungsten ratio $x = 0.1$, the plot shows the co-existence of the spin-wave-like excitation and non-coherent excitations.

The dynamic structure factor is computed by $S(\mathbf{k}, \omega) = |\mathbf{S}(\mathbf{k}, \omega)|^2$. The results are exhibited in two ways: (1) the dynamic structure factor over the high symmetry path $\Gamma \to M \to K$, and (2) the powder average over the one or several more planes along with the reciprocal vector $\mathbf{R}$ spanning the lattice. As is shown in 3.5, the structures of coherent quasi-particle dispersion

can be seen at high energies for $\mathcal{S}(k,\omega)$ at low temperatures for the systems with three different tungsten ratios (0.1, 0.3 and 0.5). The spin-wave-like dispersion shown in figure 3.5 (left) for the setting W ratio = 0.1 is likely the remaining antiferromagnetic dispersion, while the spin-wave-like dispersion shown in figure 3.5 (right) for the setting W ratio = 0.5 is likely the remnant of columnar antiferromagnetic order from the J_2 dominating case. Interestingly, low energy incoherent excitations are very strong. In the plot of tungsten ratio W ratio = 0.1, the strength of the incoherent excitation even overshadows the dispersion lines radiating from the low energy area in the M point (3.5 (left). To highlight the dispersion relation, we manipulated the data by times the dynamics structure factor by ω and ω^2: $S''(k,\omega) := \omega \cdot S(k,\omega)$ and $S''(k,\omega) := \omega^2 \cdot S^2(k,\omega)$. The dispersion relation originating from the low energy area in M point can be clearly seen in the diagram 3.6.

The coexistence of spin-wave-like excitation and incoherent excitations can be observed more clearly in the cross sectional k_x - k_y plot of the dynamics structure factors. We used the spin configurations of 120×120 to conduct the LLD calculations, and plotted the k_x-k_y cross sections of $S(k,\omega)$ in the energy level $\omega = 0, 10,$ and 20 respectively. In the energy region $\omega = 10$ (figure 3.7), we can see that even in a tungsten setting as low as 10%, the spin-wave-like dispersion is displayed as excitations forming in the shapes of circles, accompanied by strong incoherent excitations. We choose three points on the high symmetry path to illustrate the strength of incoherent excitations in low energy area, as shown in figures 3.8 and 3.9. It is interesting to see that high energy spin-wave-like dispersion survives the strong incoherent excitations.

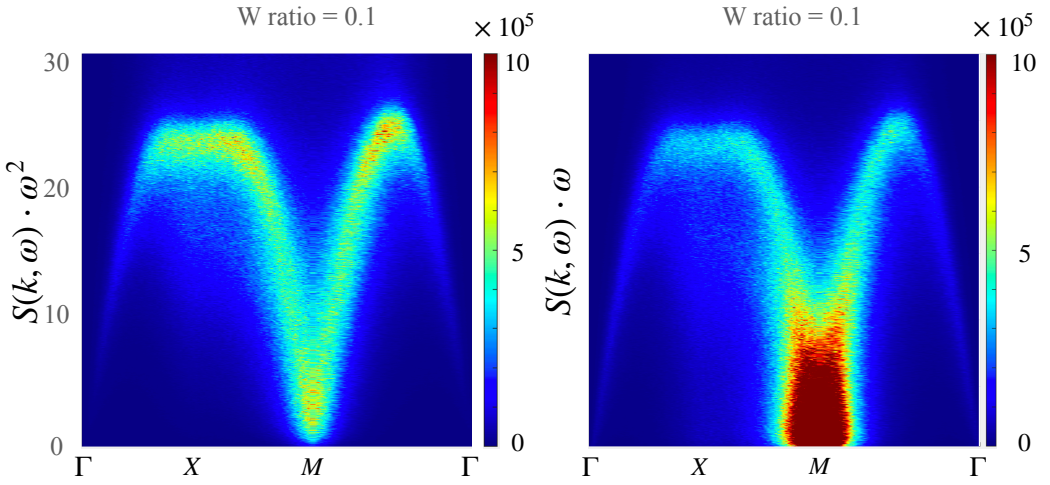

Figure 3.6: Highlighted dynamic structure factor against k values on the high symmetry path Γ-X-M-Γ, simply by multiplying $S(k,\omega)$ by ω or ω^2. Evidently the spin-wave-like excitations can be traced back to Γ point at low energy levels.

The nature of the incoherent excitations can be explained by the Halperin-Saslow theory. Halperin and Saslow (HS) pointed out that a system with static moments can support low-energy hydrodynamics modes [93, 94, 95]. Since spin glass order can be treated as a presence of static moments in the ground state, and also, since the spins in glass order have zero magnetization, for such kind of systems, HS theory predicts that there exists linearly dispersing modes such that $\omega = vk$, with velocity $v = \gamma\sqrt{\rho_s/\chi}$, where χ is the spin susceptibility and ρ_s is the spin stiffness. Such a dispersion relation tells us the density of states, and consequently the dynamical susceptibility $\chi''(\omega) = [1 - \exp\frac{-\omega}{k_B T}] \cdot S(\omega)$, in the low energy region have a linear relation with energy level ω.

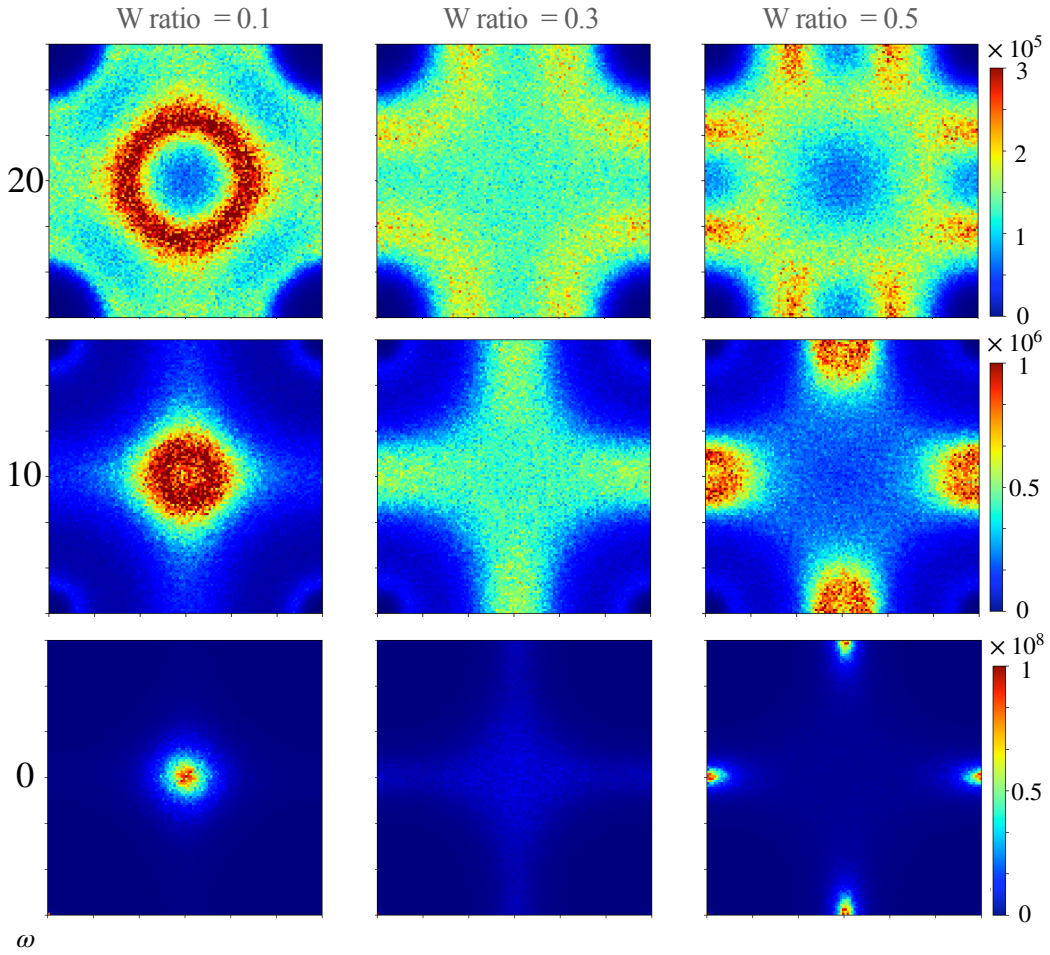

Figure 3.7: (left to right) Plots of cross sections on the k_x-k_y plane showing the structure of spin dynamics structure factor in a L = 120 square lattice with tungsten ratio = 0.1, 0.3 and 0.5 at fixed energy levels $\omega = 0$, $\omega = 10$ and $\omega = 20$, from bottom to top respectively.

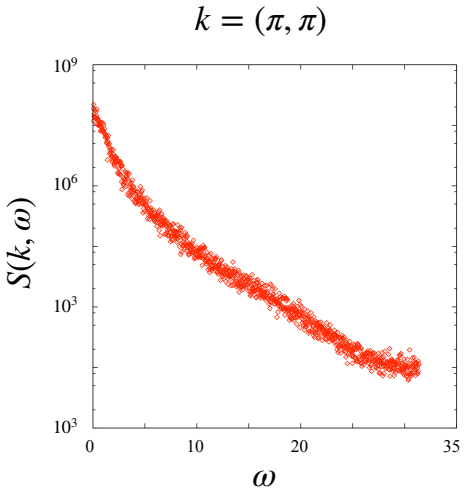

Figure 3.8: Dynamic structure factor against energy level ω values at the $(\mathbf{k} = \pi, \pi)$.

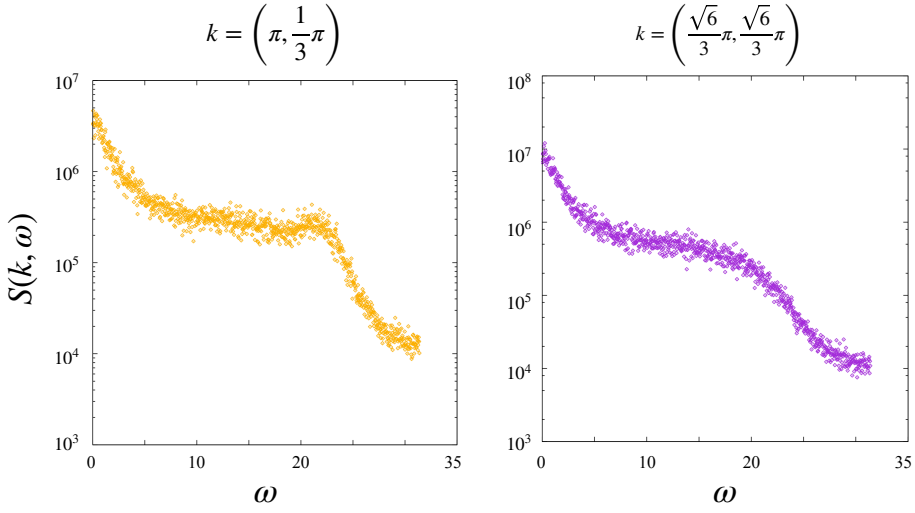

Figure 3.9: Dynamic structure factor against energy level ω values for two k vectors around the $(\mathbf{k} = \pi, \pi)$ on the high symmetry path.

Chapter 4

Machine learning phases of matter: Scalability and limitations

As was discussed in the introduction, since system configurations of magnetic systems can be technically treated as or be reconstructed to 2D or 3D images, there is no surprise they can be processed in a similar fashion of how images being processed today — by using the machine learning techniques, especially neural networks, desired features can extracted in a moment of blinkering. Normally, extensive physics quantities can be seen as such features. In this chapter, we focus on how to use machine learning techniques to deal with locality of these extensive physics parameters.

In order to deal with locality appropriately, we constructed a special purpose machine learning framework. Figure 4.1 presents a schematic diagram

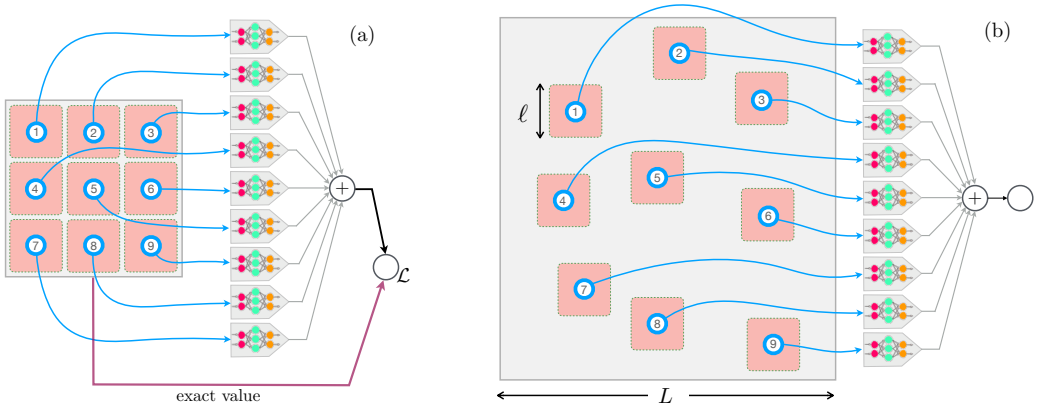

Figure 4.1: (a)Configurations are sliced into non-overlapping segments — focuses before being added descriptors and sent into NN. Then focuses will be used to train the NN. The neural network will back-propagate only until the results from all focuses of the configuration have been considered. (b) For the application of NN to large systems, the focuses are selected from the configuration with random cut points. The predicting result is an average over predictions of these selected focuses.

for our framework. The framework's purpose is to translate a system configuration of a specific physics model into a numerical value(s) representing extensive parameters such as energy density and binary output referring to specific phases. The framework consists of three basic components: the first component cuts each system configuration into equal length non-overlapping segments (4.1 (a)); the second component adds descriptors to these segments with respect to the symmetry group relating to the particular model; the last component is the NN that uses the previously processed data segments as training data and then aims to use the model for predicting desired physical quantities. The goal of the framework is to use the NN for predictions on various lattice models, with only a moderate amount of adaptions of the NN

models. We will discuss the functions of each part in details in the following paragraphs.

4.1 Data Pre-processing and Descriptors

Before training neural network to learn the features of spin configurations, we need to pre-processed datasets according to the geometry of the physics model. We used a method similar to the EDNN to enable the NN to learn the features of whole system configuration of the particular model. As is shown in figure 4.1(a), configurations were cut into non-overlapping segments with focal length f (the side length in most cases), and we defined each of them as focus. The shape of focuses is determined by the type of Bravais lattice of the model that the NN is being applied. For example, the model will cut square lattice Ising system configurations into square focuses, as is hown in figure 4.2. In this case, each spin in the system is referred as σ_j, pointing up or down. Evidently, we can acquire focuses in a number to the order of L^2/f^2 from one single system configuration with lattice length L. Then the cut focuses will be added descriptors before being sent into neural network.

The next step is to add descriptor on to each of focuses. Here we continue to use the Ising system as example. A descriptor is used to construct effective coordinates $\{G_l\}$ from focuses from the specific system configurations $\{\sigma_j\}$ up to a cutoff to the focus size, where these feature variables $\{G_l\}$ are input to the NN which predicts the specific physical quantities at the output [96, 97, 98]. Since the physical quantities of the system, such as phase and energy

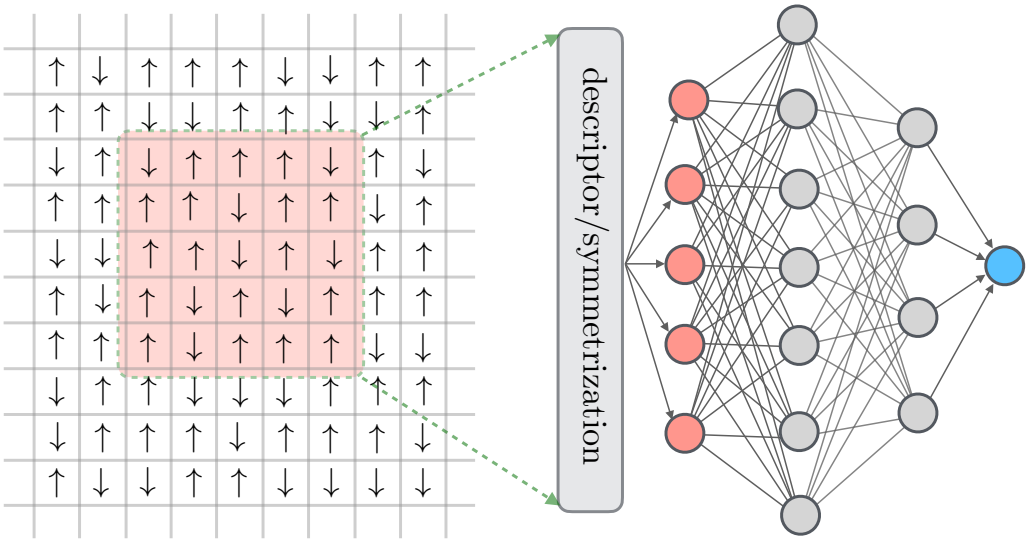

Figure 4.2: Machine learning model for phase classification or energy prediction of two-dimensional Ising model. Descriptors are added to datasets to respect the corresponding symmetry group.

density, are invariant under a operation of the lattice symmetry group, the goal of the effective coordinates $\{G_l\}$ is to provide a neighborhood environment information that is constant under the same operation, such as rotate 90° around z-axis of the center. First of all, the standard procedure that decompose the spin configuration $\{\sigma_j\}$, a high-dimension reducible representation of the lattice information, is transforming it into a basis that consists of the irreducible representations (irreps), where this basis's matrix that represents the spin configuration $\{\sigma_j\}$ is decomposable and automatically block-diagonalized due to the lattice geometry. In accord, this basis will be transformed with the formula given in the character table of point group.

Instead of the power-spectrum and bispectrum, we introduce a descriptor modified from the bispectrum method that is calculated by the reference basis functions $\boldsymbol{f}^{\Gamma}_{\text{ref}}$. By averaging each $\{\sigma_j\}$'s surrounding in the particular configuration, we can compute the reference basis functions so that they are less sensitive to the small variation in the neighborhood spin configurations. Then, we can define the effective coordinates $\{G_l\}$ as $\{\eta^{\Gamma}_r\}$, where $\eta^{\Gamma}_r = \boldsymbol{f}^{\Gamma}_{\text{ref}} \cdot \boldsymbol{f}^{\Gamma}_r$.

In summary, our whole procedure can be simplified as the following formula:

$$\{\sigma_j\} \;\rightarrow\; \{\boldsymbol{f}^{\Gamma}_r\} \;\rightarrow\; \{\eta^{\Gamma}_r\}$$

For example, figure 4.3(a), the four sites are the 3^{3rd} nearest-neighbors to the center, and they can be decomposed by: $4 = A_1 \oplus B_2 \oplus E$ in the discrete lattice symmetry group D_4. The irreps basis are:

$$f^{A_1} = \sigma_1 + \sigma_2 + \sigma_3 + \sigma_4$$

$$f^{B_2} = \sigma_1 - \sigma_2 + \sigma_3 - \sigma_4$$

$$\boldsymbol{f}^{E} = (\sigma_1 - \sigma_3,\ \sigma_2 - \sigma_4)$$

While in the figure 4.3(b), these eight sites Ising variables are the 4^{th} nearest neighbor and they can be readily decomposed through: $8 = A_1 \oplus A_2 \oplus B_1 \oplus B_2 \oplus 2E$ The corresponding irreps basis are:

$$f^{A_1} = \sigma_1 + \sigma_2 + \sigma_3 + \sigma_4 + \sigma_5 + \sigma_6 + \sigma_7 + \sigma_8$$

$$f^{A_2} = \sigma_1 - \sigma_2 + \sigma_3 - \sigma_4 + \sigma_5 - \sigma_6 + \sigma_7 - \sigma_8$$

$$f^{A_3} = \sigma_1 + \sigma_2 - \sigma_3 - \sigma_4 + \sigma_5 + \sigma_6 - \sigma_7 - \sigma_8$$

$$f^{A_4} = \sigma_1 - \sigma_2 - \sigma_3 + \sigma_4 + \sigma_5 - \sigma_6 - \sigma_7 + \sigma_8$$

$$\boldsymbol{f}^{E_1} = (\sigma_2 - \sigma_3 - \sigma_6 + \sigma_7,\ \sigma_1 + \sigma_4 - \sigma_5 - \sigma_8)$$

$$\boldsymbol{f}^{E_2} = (\sigma_1 + \sigma_2 - \sigma_5 - \sigma_6,\ \sigma_3 + \sigma_4 - \sigma_7 - \sigma_8)$$

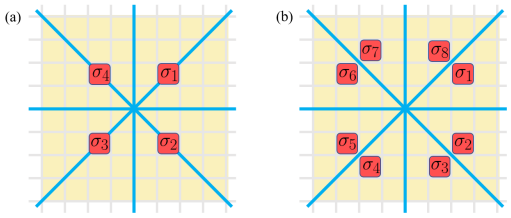

Figure 4.3: The examples of a block of the Ising configuration $\{\sigma_j\}$ that are used to generate block-diagonal representations of the D_4 point group of square lattice. (a) This four sites are the 3^{rd} nearest-neighbor to the center. (b) This eight sites are the 4^{th} nearest-neighbor.

Once the dataset is altered to the extent that the related symmetry group is fully respected, we can finally move on to the step of training neural net-

works for predicting desired physical quantities. The aforementioned EDNN approach, and our method here, can both be seen as variants of the batch training method widely used in the machine learning area. Batch training is the practice that divides the dataset into several equal length sub-datasets (batches), and that only updates model after all training samples in one batch have been evaluated. By contrast if the NN model is updated right after each time a training sample has been evaluated, such practice uses a so-called stochastic gradient descent. The main purpose of batch training is to minimize training error by acquiring a smoother gradient descent curve. Therefore, choosing batch size is a balancing act between maximizing prediction accuracy and training speed. We use batch training for gradient descent but each batch only consists of focuses from only one system configuration, so the contributions of these focuses can be evaluated with the training label associated to the configuration. Thus, we can force the NN to learn the structural characteristics of this physics model under the same specific conditions.

Furthermore, data used for predictions are pre-processed in a similar fashion like the method for training purposes, but there is a small but noticeable difference: instead of averaging the aggregated sum of contributions of focuses all over the configuration, the focuses for predictions are randomly selected with random cutting points from a system configuration (figure 4.1(b)) and then an average is computed. This is simply to make sure the neural network can predict with random input form an arbitrarily large configurations.

4.2 Application to 2D Ising model

As we discussed in the introduction, NNs have been proven their ability to effectively detect the phase of Ising models. In the time since Carrasquilla and Melko laid down the ground work, further efforts to exploit machine learning's potential on Ising systems have followed [99, 100, 101, 102, 103, 104, 105]. For example, there is a study that a trained neural network to classify phases of configurations based on their energy levels and magnetization operators. Another study used the correlation functions defined on each spin as input to train the neural network. Methods in this area of studies are not just limited to deep neural networks. Other machine learning models have also been used by researchers on Ising models. For example, Restricted Boltzmann Machine has been used to capture the temperature dependence of magnetization, energy and spin correlations of Ising configurations. Principal Component Analysis was used as an unsupervised learning method to discover phase transitions of Ising system, and a Support Vector Machine was employed to learn the mathematical form of physical discriminators such as order parameters of Ising systems.

Before we move on the topic of our predictions, it is necessary to briefly introduce the physics property of Ising model. The Ising model is a binary-state spin (σ) model with $\sigma = \pm 1$ with a Hamiltonian written as:

$$\mathcal{H} = -J \sum_{<ij>} \sigma_i \sigma_j, \tag{4.1}$$

where the summations are over the nearest neighbor pairs, and J refers to

the interaction strength between spins. The basic configuration of an Ising model is an $L \times L$ grid of discrete interacting spins that are either pointing up (σ = 1) or pointing down (σ = -1). Although the Ising model is easy to define, its behaviors can be rich. We can set an Ising system to ferromagnetic or anti-ferromagnetic simply by manipulating the values of J. A positive value of J indicates to ferromagnetic and a negative value of J refers to anti-ferromagnetic. The canonical Ising model defined by periodic boundary conditions exhibits continuous phase transition around a critical temperature T_C = 2.269. Besides the very particular point at the critical temperature, configurations of the Ising model are considered to belong exclusively to the one of two phases. At temperatures below T_C, most of spins in the system would align to each other and the system would behave in an orderly way. On the other hand, the system would behave in a highly disorderly way, such that spin-ups and spin-downs are roughly equal in numbers when the temperature is above T_C.

4.2.1 Energy Density Predictions

The specific model designed for energy density prediction is a convolutional neural network (CNN) model. CNN is a type of neural network based on the shared-weight architecture of the convolutional filters process input features by smoothly sliding over the input, and thus provide translational equivariant responses [106]. This property enables CNN to capture the structural characters of the images and other 2D/3D objects. In our case, since the configurations and also the focuses of the Ising system can be treated as monochromatic

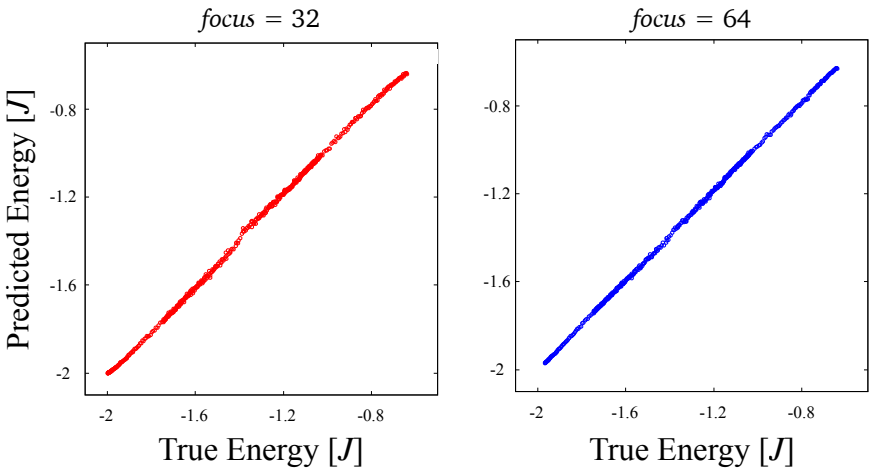

Figure 4.4: Energy density estimation by NN vs. the exact energy density extracted from Monte-Carlo simulations.

images, we can utilize CNN's advantages to help us better understand the mapping between local structure and extensive parameters.

Basically, our model consists of two convolutional layers of size $c \times c$ and five fully connected layers, and all the layers employ ReLU to be its activation function. Activation function is a type of function that allows neural networks to have the capability to fit nonlinear functions. The convolutional filters have unit stride and hence preserve the resolutions of the input data. Each of convolutional layers is followed by a 2×2 max pooling layer to enhance its structural characteristics. Each focus would be reduced to the size of $(f - c + 1)/2$ before being put into the first fully connected layer. The number of input nodes in the first fully connected layer is proportional to the reduced focus size with a fixed ratio. The fully connected layers would reduce data exponentially until the output layer generates a single numerical value. The NN repeats the preceding procedures until energy contributions from all focuses are averaged, and a $L1$ loss function is used to compute the mean absolute error between the averaged focus contribution and the exact energy density extracted from Monte-Carlo simulations. Moreover, a standard Adam optimizer is used to regulate the training process, together with a global learning rate 0.001. In addition, a dropout layer with dropout probability 0.2 is implemented before the output layer. Dropout layer is a simple way to prevent the model from over-fitting the dataset [107]. All those neural networks are trained with same number of iterations.

Training of the model was executed by a computer hosting multiple graphic processing units (GPUs). We used the PyTorch library to realize our model

and to enable the model's ability to utilize the GPUs in parallel. In the training process, $40,000$ Ising system configurations of lattice length $L = 320$ were used to train the neural network and another $8,000$ Ising system configurations were used for predictions. These configurations will be used multiple times for all focus sizes. Ranging from 16 to 80, as for each focus size, there is a number $40,000 \cdot L^2/f^2$ focuses constituting a training dataset for the model specific to this size. Since focuses from one configuration compose one batch, the total number of batches will also be $40,000$, and the model will iterate the training process over all the batches by 40 epoches. Once the training process stabilizes at a reasonable loss rate, the model is ready to be used for predictions.

For the temperature range $T = 2.2$ and focus size of 32, the neural network's prediction accuracy on energy achieves an accuracy of 97.5%, resulting in a mean square error of $0.012J/L^2$. As is shown in Figure 4.4, the prediction accuracy improves when the size of focuses increases to 64. For the same temperature at $T = 2.2$, the prediction accuracy reaches 99.8% for $f = 64$. It is noteworthy that the model tends to overestimate the energy density right above the critical temperature and to underestimate the energy right below. This systematic error persists in predictions based on small focuses. For example, error is more prevalent in the predictions of $f = 32$ than in predictions of $f = 64$. Evidently, systematic error could limit the NN's accuracy in predictions, especially when one uses a small segment of data to predict a system with large configuration. Hence, we may reckon that, among the abundant information that $f = 64$ focus contains that the neural network could learn to improve its prediction quality, what is the particular on that can help $f = 64$

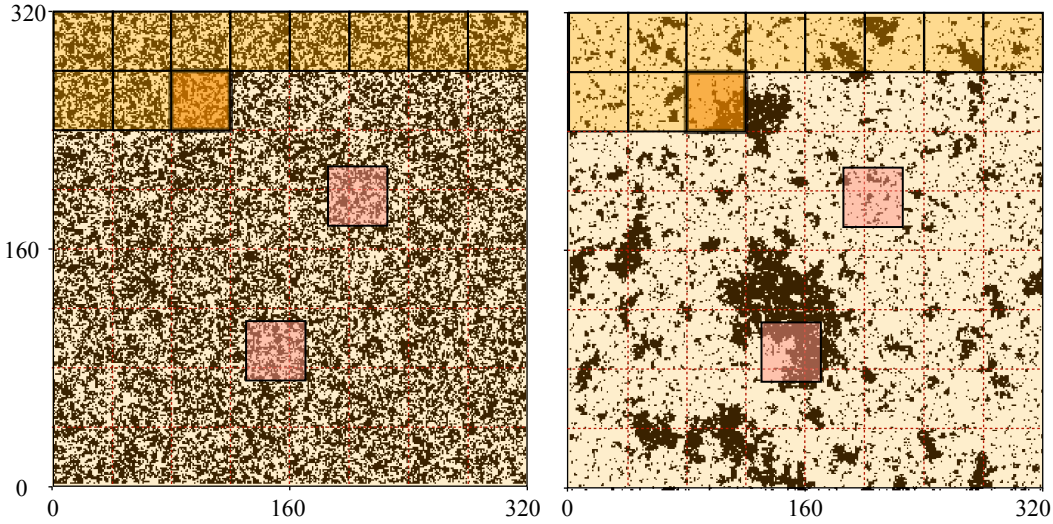

Figure 4.5: Focus's coverage of correlation length. The system configuration shown in left is captured at T = 4.2 and the right one is captured at T = 2.27.

prediction reducing the systematic error? The quality that is directly related to system size is the correlation length of spins.

4.3 Scalability and Correlation Length

Correlation length is the measurement of how much the spins σ_i and σ_j at two sites are correlated, especially when two spins are far apart. A simple measurement of spin correlation can be written as:

$$< \sigma_j; \sigma_j >:=< \sigma_i \sigma_j > - < \sigma_i >< \sigma_j > \tag{4.2}$$

Spin correlation would be zero if all the spins were independent of each other. This formula is called truncated correlation function and decays exponentially

as $|i-j| \to \infty$ so $< \sigma_j; \sigma_j > \sim \exp(-|i-j|/\xi)$. The quantity ξ is the length scale which is called the correlation length. A short correlation length suggests that the distant spins in the system are weakly correlated, and near spins are strongly correlated. In general, locality is inversely correlated with correctional length. If larger locality were exist in the system, the correlation length would correspondingly become shorter. Moreover, the correlation length grows algebraically when temperature approaches the phase transition and it will approach infinity at the phase transition. As was discussed previously, the accuracy of the neural network is partly determined by the amount of information contained in focus, and locality determines how much a physics quantity is influenced by local neighborhood. Therefore, by using limited size focuses, NN can predict with enough accuracy when the correlation length in the system is short enough.

As is shown in figure 4.5, at a temperature close to phase transition ($T = 2.27$ for the Ising system configuration in figure 4.5(right)), correlations between spins are strong, and so small-sized focuses cannot contain their interactions. While for a temperature well above the phase transition, ($T = 4.2$ in figure 4.5(left)), the spins are only correlated to each other locally, so small-sized focuses can well contain the information of distant interactions, and thus, the local structure can well reflect the extensive parameters of the whole configuration. On the other hand, since it is impossible for a NN to learn all the features of an Ising system in the adjacency of phase transition through training samples of limited system sizes, the NN would lose a considerable portion of its accuracy in predictions made for temperatures around the phase

transition due to focuses' lack of information of correlation length.

From the perspective of batch training, choosing a smaller size for f results in more square segments for which the model can parallelize computations more efficiently. In view of the fact that the learning curve becomes flattened if the focus size goes beyond the length scale, the choosing of sizes of focuses and consequently sizes of batches also needs to contemplate focus's coverage of correlation length. We chose several focus sizes and examine them in a naive neural network model to test their coverage of correlation length in a stochastic training way. Then we conducted a full scale NN test with the range of these focuses. The sizes of focuses covered in this study are 16, 20, 32, 40 and 80.

4.3.1 Phase Classification Results

The specific neural network model used for phase classifications includes functions and parameters similar to ones used in the energy density prediction model, including the dropout layer, ReLU functions followed by each layer, and hyper-parameters such as learning rate. The model consists of one non-reducing and five reducing fully connected layers. The model will finally outputs a single digit, zero or one, of which determines the phase of input systems. Therein, zero refers that the system is in ferromagnetic order and one refers that the system is in disordered state, respectively. The neural network repeats the preceding procedures until contributions from each focus of one single Ising configuration are averaged and used for calculating loss functions. Since the samples are assigned one of two labels, we implemented the binary cross en-

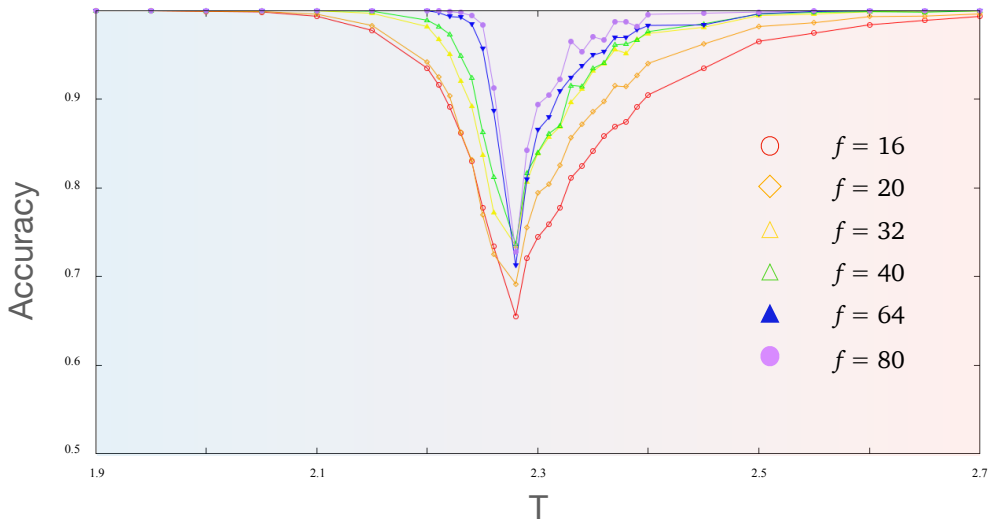

Figure 4.6: Preliminary phase prediction results corresponding to the input data without added descriptors.

tropy loss function, BCELogits, in our neural network. BCELogits calculates a value summarizing the average difference between the actual and predicted probability distribution for predicting class 1. The goal is to minimize this value. A perfect cross-entropy value is 0. To minimize the loss function, an Adam optimizer is used to accompany with the loss function. Same as in the energy estimation model, the dropout layer is added before the output layer with dropout probability set to 0.2 and global learning rate is 0.001.

Figure 4.6 shows preliminary results of phase predictions, in which we did not add descriptors to the input focus data. The model has already shown its distinguishing ability with more than 90% correction rate for temperatures above 2.5 and below 2.2.

As is shown in 4.7(top), the results show that for any size of focus, the accuracy of classification results deteriorates rapidly when the temperatures approach to phase transition from either side. As expected, at a given temperature and for a given arbitrarily large system configuration, the classification accuracy of NN when using smaller focuses is equal to, or lower than, the accuracy when using larger focuses. Furthermore, the extent of deterioration differs depending on the sizes of the focuses. Evidently, the accuracy of classifications based on small sizes of focuses deteriorates faster than that with classifications based on larger sizes. The results suggest there may exists a focus size dependent re-scaling relation and thus the results may have a same universal physics. Assuming the scenario, we speculate the relation between focus sizes and the extents of the deterioration of prediction accuracy behaves

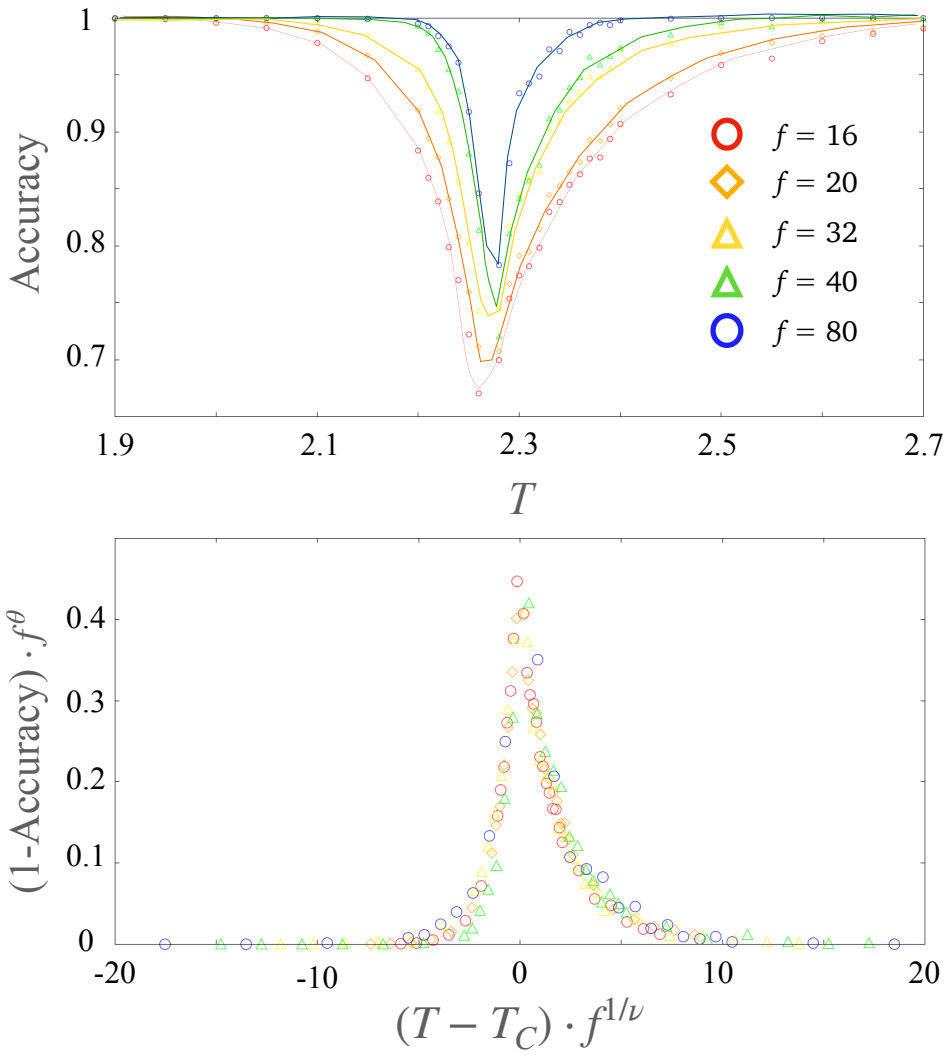

Figure 4.7: Top: Phase prediction results by our fully connected neural network model. Bottom: Scaling collapse of $(1-\text{Accuracy})\cdot L^{\theta}$ in the form Eq.4.3 with the critical exponent $\nu = 1$.

in the following way:

$$(1 - \text{Accuracy}) \cdot L^{\theta} = \mathcal{F}((T - T_C) \cdot L^{1/\nu}), \tag{4.3}$$

where $\mathcal{F}$ is an universal function, the critical exponent ν relates to the size of correlations to the temperature.Same as the transition temperature, the critical exponent ν has been well studied before for 2-dimensional Ising model and it is accordingly to 1. θ is a new exponent that we introduce to relate the size of correlations to the sizes of focuses. We infer the new exponent θ from the behavior of the classification accuracy. The data collapse of $(1-\text{Accuracy}) \cdot L^{\theta}$ in figure 4.7 (bottom) finally gives the value θ to be 0.11.

In order to further prove the power law decay relation of the classification accuracy and focus sizes, we measured the width of temperature windows for difference focus sizes at a given accuracy level. Since the correlation length ξ can be expressed as:

$$\xi \sim \frac{1}{|T - T_C|^{\nu}} \tag{4.4}$$

from this relation, we can define a linear formula between temperature cut-offs of the accuracy measurement and scaled focus sizes:

$$T^* = T_C \pm C \cdot f^{-1/\nu} \tag{4.5}$$

where C is a constant, T^* is a customized cut-off temperature. As is shown in 4.8, at the accuracy levels 85% and 90%, the quantity $\Delta T = 2 \cdot |T^* - T_C|$ is almost perfectly linear to the scaled focus size $f^{-1/\nu}$, which further proves the

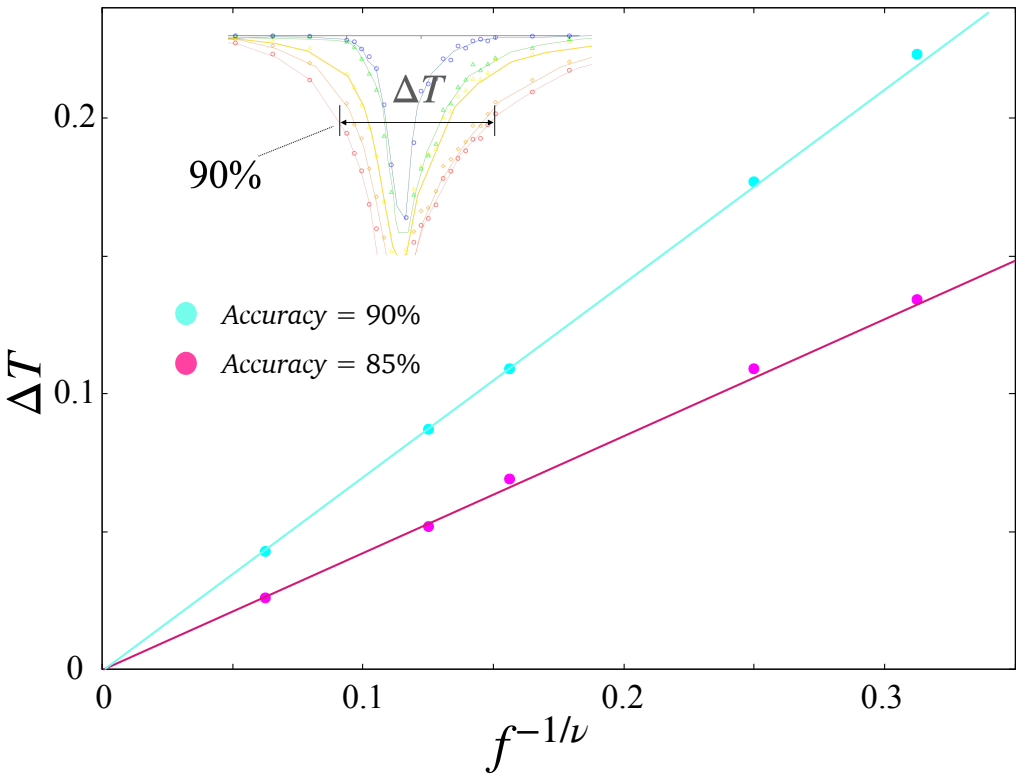

Figure 4.8: ΔT vs. $f^{-1/\nu}$ at the accuracy levels 85% and 90%, showing the result can be well extrapolated linearly.

existence of the scale invariant exponent θ.

4.4 Discussion and outlook

In this work we designed a machine learning framework to accurately predict extensive parameters and we use it to classify spin-model configurations and to predict their energy density. The framework is scalable that it can predict systems of arbitrary sizes. The NN model in our framework can estimate energy density highly accurately. Furthermore, we have illustrated the accuracy

limitation of phase classifications by using limited size focuses as input. Then we did a exponent collapse study to investigate the relation of focus sizes and prediction accuracy. We discovered a new exponent θ to relate the size of correlations to the sizes of focuses, and numerically proved that the prediction accuracy is directly influenced by correlation length.

Besides the model's distinguishing ability over different focuses can also give use insights about the type of phase transitions. Power law decay of correlation near criticality is one important property of second order phase transitions. If we can use this power law decay relation extracted by ML methods, it may give us an insight of how to determine the type of phase transition.

Bibliography

[1] C. Lacroix, P. Mendels, and F. Mila, eds. *Introduction to Frustrated Magnetism: Materials, Experiments, Theory*. Series in Solid-State Sciences. Springer, 2011.

[2] R. Moessner and A. P. Ramirez. "Geometric frustration". In: *Physics Today* 184.3 (Mar. 2006), pp. 557–564.

[3] D. Marx and J. Hutter. *Introduction to Frustrated Magnetism*. Ed. by Fre de ric Mila Claudine Lacroix and Philippe Mendels. Springer, 2011.

[4] J. T. Chalker, P. C. W. Holdsworth, and E. F. Shender. "Hidden order in a frustrated system: Properties of the Heisenberg Kagome antiferromagnet". In: *Phys. Rev. Lett.* 100.855 (1992).

[5] M. E. Zhitomirsky. "Octupolar ordering of classical kagome antiferromagnets in two and three dimensions". In: *Phys. Rev. B* 78 (2008), p. 094423.

[6] G.-W. Chern and R. Moessner. "Dipolar Order by Disorder in the Classical Heisenberg Antiferromagnet on the Kagome Lattice". In: *Phys. Rev. B* 110 (2013), p. 077201.

[7] R. Moessner and J. T. Chalker. "Properties of a Classical Spin Liquid: The Heisenberg Pyrochlore Antiferromagnet". In: *Phys. Rev. Lett.* 80.2929 (1998).

[8] R. Moessner and J. T. Chalker. "Low-temperature properties of classical geometrically frustrated antiferromagnets". In: *Phys. Rev. B.* 58 (1998), p. 12049.

[9] A. P. Bartók et al. "Gaussian Approximation Potentials: The Accuracy of Quantum Mechanics". In: *Phys. Rev. Lett.* 104 (2010), p. 136403.

[10] Z. Li, J. R. Kermode, and A. De Vita. "Molecular Dynamics with On-the-Fly Machine Learning of Quantum-Mechanical Forces". In: *Phys. Rev. Lett.* 114 (2015), p. 096405.

[11] Jonas Greitemann et al. "Identification of emergent constraints and hidden order in frustrated magnets using tensorial kernel methods of machine learning". In: *Phys. Rev. B.* 100 (2019), p. 174408.

[12] Siyu He et al. "Learning to predict the cosmological structure formation". In: *Proc. Natl. Acad. Sci. U.S.A.* 116.28 (2019), p. 13825.

[13] Nicholas Lubbers, Turab Lookman, and Kipton Barros. "Inferring low-dimensional microstructure representations using convolutional neural networks". In: *Phys. Rev. E.* 96 (2017), p. 052111.

[14] Kyle Mills, Corneel Casert, and Isaac Tamblyn. "Adversarial Generation of Mesoscale Surfaces from Small-Scale Chemical Motifs". In: *J. Phys. Phys. Chem.* 124.42 (2020), p. 23158.

[15] J. C. Snyder et al. “Finding Density Functionals with Machine Learning”. In: *Phys. Rev. Lett.* 108 (2012), p. 253002.

[16] J. Behler and M. Parrinello. “Generalized Neural-Network Representation of High-Dimensional Potential-Energy Surfaces”. In: *Phys. Rev. Lett.* 98 (2007), p. 146401.

[17] Xiao-Yu Dong, Frank Pollmann, and Xue-Feng Zhang. “Machine learning of quantum phase transitions”. In: *Phys. Rev. B* 99 (2019), p. 121104.

[18] Juan Carrasquilla and Roger G. Melko. “Machine Learning phases of Matter”. In: *Nat. Phys* (2017), p. 4035.

[19] K. Mills et al. “Extensive deep neural networks for transferring small scale learning to large scale systems”. In: *Chem. Sci.* 10 (2019), p. 4129.

[20] M. Hermanns, I. Kimchi, and J. Knolle. “Physics of the Kitaev Model: Fractionalization, Dynamic Correlations, and Material Connections”. In: *Annu. Rev. Condens. Matter Phys.* 9.17 (2018).

[21] H. Takagi et al. “Concepts and realization of Kitaev quantum spin liquids”. In: *Nat. Rev. Phys.* 1 (2019), p. 264.

[22] J. Nasu, M. Udagawa, and Y. Motome. “Vaporization of Kitaev spin liquids”. In: *Phys. Rev. Lett.* 113 (2014), p. 197205.

[23] S. Trebst. “Kitaev Materials”. In: *arXiv* 1701.07056 (2017).

[24] A. Kitaev. “Anyons in an exactly solved model and beyond”. In: *Ann. Phys. (Amsterdam)* 321.2 (2006).

[25] G. Jackeli and G. Khaliullin. "Mott Insulators in the Strong Spin-Orbit Coupling Limit: From Heisenberg to a Quantum Compass and Kitaev Models". In: *Phys. Rev. Lett.* 102 (2009), p. 017205.

[26] J. Chaloupka, G. Jackeli, and G. Khaliullin. "Kitaev-Heisenberg Model on a Honeycomb Lattice: Possible Exotic Phases in Iridium Oxides A_2IrO_3". In: *Phys. Rev. Lett.* 105 (2010), p. 027204.

[27] J. Chaloupka, G. Jackeli, and G. Khaliullin. "Zigzag Magnetic Order in the Iridium Oxide Na_2IrO_3". In: *Phys. Rev. Lett.* 110 (2013), p. 097204.

[28] J. G. Rau, E. K.-H. Lee, and H.-Y. Kee. "Generic Spin Model for the Honeycomb Iridates beyond the Kitaev Limit". In: *Phys. Rev. Lett.* 112 (2014), p. 077204.

[29] Y. Sizyuk et al. "Importance of anisotropic exchange interactions in honeycomb iridates: Minimal model for zigzag antiferromagnetic order in Na_2IrO_3". In: *Phys. Rev. B* 90 (2014), p. 155126.

[30] S. M. Winter, H. O. Jeschke Y. Li, and R. Valenti. "Challenges in design of Kitaev materials: Magnetic interactions from competing energy scales". In: *Phys. Rev. B* 93 (2016), p. 214431.

[31] L. Janssen, E. C. Andrade, and M. Vojta. "Magnetization processes of zigzag states on the honeycomb lattice: Identifying spin models for α-$RuCl_3$ and Na_2IrO_3". In: *Phys. Rev. B* 96 (2017), p. 064430.

[32] S. M. Winter et al. "Models and materials for generalized Kitaev magnetism". In: *J. Phys.: Condens. Matter* 29 (2017), p. 493002.

[33] P. P. Stavropoulos, D. Pereira, and H.-Y. Kee. "Microscopic Mechanism for a Higher-Spin Kitaev Model". In: *Phys. Rev. Lett.* 123 (2019), p. 037203.

[34] T. Moriya. "Anisotropic Superexchange Interaction and Weak Ferromagnetism". In: *Phys. Rev.* 120.91 (1960).

[35] I. Rousochatzakis and N. B. Perkins. "Classical spin liquid instability driven by off-diagonal exchange in strong spin-orbital magnets". In: *Phys. Rev. Lett.* 118 (2017), p. 147204.

[36] P. Saha et al. "Hidden Plaquette Order in a Classical Spin Liquid Stabilized by Strong Off-Diagonal Exchange". In: *Phys. Rev. Lett.* 98 (2019), p. 045121.

[37] A. M. Samarakoon et al. "Classical and quantum spin dynamics of the honeycomb Γ model". In: *Phys. Rev. B* 98 (2018), p. 045121.

[38] S. Elitzur. "Impossibility of spontaneously breaking local symmetries". In: *Phys. Rev. D* 12 (1975), p. 3978.

[39] M. E. Zhitomirsky. "Field-induced transitions in a kagome antiferromagnet". In: *Phys. Rev. Lett.* 88 (2002), p. 057204.

[40] K. Penc, N. Shannon, and H. Shiba. "Half-Magnetization Plateau Stabilized by Structural Distortion in the Antiferromagnetic Heisenberg Model on a Pyrochlore Lattice". In: *Phys. Rev. Lett.* 93 (2004), p. 197203.

[41] M. E. Zhitomirsky, A. Honecker, and O. A. Petrenko. "Field induced ordering in highly frustrated antiferromagnets". In: *Phys. Rev. Lett.* 85 (2000), p. 3269.

[42] L. Seabra et al. "Novel phases in a square-lattice frustrated ferromagnet: $\frac{1}{3}$-magnetization plateau, helicoidal spin liquid, and vortex crystal". In: *Phys. Rev. B* 93 (2016), p. 085132.

[43] J. Schulenburg et al. "Macroscopic Magnetization Jumps due to Independent Magnons in Frustrated Quantum Spin Lattices". In: *Phys. Rev. Lett.* 88 (2002), p. 167207.

[44] N. A. Fortune et al. "Cascade of Magnetic-Field-Induced Quantum Phase Transitions in a Spin-$\frac{1}{2}$ Triangular-Lattice Antiferromagnet". In: *Phys. Rev. Lett* 87 (2001), p. 097203.

[45] J. Alicea, A. V. Chubukov, and O. A. Starykh. "Quantum stabilization of the 1/3-magnetization plateau in Cs_2CuBr_4". In: *Phys. Rev. Lett.* 102 (2009), p. 137201.

[46] J. Wosnitza, S.A. Zvyagin, and S. Zherlitsyn. "Frustrated magnets in high magnetic fields – selected examples". In: *Rep. Prog. Phys.* 102 (2009), p. 137201.

[47] G. Misguich, Th. Jolicoeur, and S. M. Girvin. "Magnetization Plateaus of $SrCu_2(BO_3)_2$ from a Chern-Simons Theory". In: *Phys. Rev. Lett.* 87 (2001), p. 097203.

[48] A. Sen, K. Damle, and A. Vishwanath. "Magnetization Plateaus and Sublattice Ordering in Easy-Axis Kagome Lattice Antiferromagnets". In: *Phys. Rev. Lett.* 87 (2001), p. 097203.

[49] R. Yadav et al. "Kitaev exchange and field-induced quantum spin-liquid states in honeycomb α-$RuCl_3$," in: *Sci. Rep.* 6 (2016), p. 37925.

[50] L. Janssen, E. C. Andrade, and M. Vojta. "Honeycomb-Lattice Heisenberg-Kitaev Model in a Magnetic Field: Spin Canting, Metamagnetism, and Vortex Crystals". In: *Phys. Rev. Lett.* 118 (2016), p. 277202.

[51] G.-W. Chern et al. "Kitaev-Heisenberg model in a magnetic field: Order-by-disorder and commensurate-incommensurate transitions". In: *Phys. Rev. B.* 109 (2017), p. 144427.

[52] M. Gohlke, R. Moessner, and F. Pollmann. "Dynamical and topological properties of the Kitaev model in a [111] magnetic field". In: *Phys. Rev. B* 98 (2018), p. 014418.

[53] H.-Y. Lee et al. "Magnetic field induced quantum phases in a tensor network study of Kitaev magnets". In: *Nat. Commun* 11.1639 (2020).

[54] Z. X. Liu and B. Normand. "Dirac and chiral quantum spin liquids on the honeycomb lattice in a magnetic field". In: *Phys. Rev. Lett.* 120 (2018), p. 187201.

[55] Z. Zhu, I. Kimchi, and L. Fu D. N. Sheng. "Robust non-abelian spin liquid and a possible intermediate phase in the antiferromagnetic Kitaev model with magnetic field". In: *Phys. Rev. B* 97 (2018), p. 241110.

[56] C. Hickey and S. Trebst. "Emergence of a field-driven U(1) spin liquid in the Kitaev honeycomb model". In: *Nat. Commun.* 10 (2019), p. 423002.

[57] J. S. Gordon et al. "Theory of the field-revealed Kitaev spin liquid". In: *Nat. Commun.* 10 (2019), p. 2470.

[58] N. D. Patel and N. Trivedi. "Magnetic field-induced intermediate quantum spin liquid with a spinon Fermi surface". In: *Proc. Natl. Acad. Sci. U.S.A.* 116 (2019), p. 12199.

[59] L. Janssen and M. Vojta. "Heisenberg-Kitaev physics in magnetic fields". In: *J. Phys.: Condens. Matter* 31 (2019), p. 423002.

[60] C. Balz et al. "Field-induced intermediate ordered phase and anisotropic interlayer interactions in α-$RuCl_3$". In: *Phys. Rev. B* 103 (2021), p. 174417.

[61] P. M. Chaikin and T. C. Lubensky. *Principles of condensed matter physics*. Cambridge Univ. Press, 1995.

[62] M. E. Fisher and D. R. Nelson. "Spin Flop, Supersolids, and Bicritical and Tetracritical Points". In: *Phys. Rev. Lett.* 32 (1974), p. 1350.

[63] Y. Shapira and S. Foner. "Magnetic Phase Diagram of MnF_2 from Ultrasonic and Differential Magnetization Measurements". In: *Phys. Rev. B* 1 (1970), p. 3083.

[64] J. G. Rau, P. A. McClarty, and R. Moessner. "Pseudo-Goldstone gaps and order-by-quantum disorder in frustrated magnets". In: *Phys. Rev. Lett.* 121 (2018), p. 237201.

[65] J. M. Kosterlitz, D. R. Nelson, and M. E. Fisher. "Bicritical and tetracritical points in anisotropic antiferromagnetic systems". In: *Phys. Rev. B.* 13.412–432 (1976).

[66] D. P. Landau and K. Binder. "Phase diagrams and critical behavior of a two-dimensional anisotropic Heisenberg antiferromagnet". In: *Phys. Rev. B* 24.1391 (1981).

[67] Y. Okwamoto. “Phase diagram of a two-dimensional Heisenberg antiferromagnet in a magnetic field”. In: *J. Phys. Soc. Jpn.* 53 (1984), p. 2423.

[68] A. S. T. Pires. “Kosterlitz-Thouless transition in a two-dimensional isotropic antiferromagnet in a uniform field”. In: *Phys. Rev. B* 50 (1994), p. 9592.

[69] A. Cuccoli et al. “Field-induced XY behavior in the $S = \frac{1}{2}$ antiferromagnet on the square lattice”. In: *Phys. Rev. B* 68 (2003), 060402(R).

[70] M. Holtschneider, W. Selke, and R. Leidl. “Two-dimensional anisotropic Heisenberg antiferromagnet in a magnetic field”. In: *Phys. Rev. B* 72 (2005), p. 064443.

[71] R. L. Leheny et al. “Spin correlations in an isotropic spin-5/2 two dimensional antiferromagnet”. In: *Phys. Rev. Lett.* 82.418 (1991).

[72] J. L. Cardy. “General discrete planar models in two dimensions: duality properties and phase diagrams”. In: *J. Phys. A Math. Gen.* 13 (1980), p. 1507.

[73] M. S. S. Challa and D. P. Landau. “Critical behavior of the six-state clock model in two dimensions”. In: *Phys. Rev. B* 33.437 (1986).

[74] J. Wang, B. Normand, and Z.-X. Liu. “One proximate Kitaev spin liquid in the K-J-Γ Model on the honeycomb lattice”. In: *Phys. Rev. Lett.* 123 (2019), p. 197201.

[75] Q. Luo et al. “Gapless quantum spin liquid in a honeycomb Γ magnet”. In: *npj Quantum Mater.* 6.57 (2021).

[76] C. Broholm et al. “Quantum Spin Liquids”. In: *Science* 367 (2020), p. 6475.

[77] M. A. Ruderman and C. Kittel. “Indirect Exchange Coupling of Nuclear Magnetic Moments by Conduction Electrons”. In: *Phys. Rev.* 96.99 (1954).

[78] Tadao Kasuya. “A Theory of Metallic Ferro- and Antiferromagnetism on Zener’s Model”. In: *Progress of Theoretical Physics* 1 (16).

[79] Kei Yosida. “Magnetic Properties of Cu-Mn Alloys”. In: *Phys. Rev.* 106 (1957), p. 893.

[80] S F Edwards and P W Anderson. “Theory of spin glasses”. In: *J. Phys. F: Met. Phys.* 5.965 (1975).

[81] R. N. Bhatt and A. P. Young. “Numerical studies of Ising spin glasses in two, three, and four dimensions”. In: *Phys. Rev. B.* 37.10 (1988), pp. 5606–5614.

[82] Grégoire Misguich and Claire Lhuillier. *Two-Dimensional Quantum Antiferromagnet*. Ed. by H T Diep. World Scientific, 2013, pp. 235–319.

[83] Lucile Savary and Leon Balents. “Disorder-Induced Quantum Spin Liquid in Spin Ice Pyrochlores”. In: *Phys. Rev. Lett.* 118 (2017), p. 087203.

[84] Seung-Ho Baek et al. “Observation of a random singlet state in a diluted Kitaev honeycomb material”. In: *Phys. Rev. B.* 102 (2020), p. 094407.

[85] Lu Liu et al. “Random-Singlet Phase in Disordered Two-Dimensional Quantum Magnets”. In: *Phys. Rev. X.* 33 (2018), p. 041040.

[86] Vamshi M. Katukuri et al. “Exchange Interactions Mediated by Non-magnetic Cations in Double Perovskites”. In: *Phys. Rev. Lett.* 124 (2020), p. 077202.

[87] O. Mustonen et al. “Spin-liquid-like state in a spin-1/2 square-lattice antiferromagnet perovskite induced by $d^{10} - -d^0$ cation mixing”. In: *Nat. Commun.* 9 (2018), p. 1086.

[88] Xiao Hu et al. “Freezing of a Disorder Induced Spin Liquid with Strong Quantum Fluctuations”. In: *Phys. Rev. Lett.* 127 (2021), p. 017201.

[89] H. C. Walker et al. “Spin wave excitations in the tetragonal double perovskite Sr_2CuWO_6”. In: *Phys. Rev. B* 94 (2016), p. 064411.

[90] P. Babkevich et al. “Magnetic Excitations and Electronic Interactions in Sr_2CuTeO_6: A Spin 1.2 Square Lattice Heisenberg Antiferromagnet”. In: *Phys. Rev. Lett.* 117 (2016), p. 237203.

[91] Hikaru Kawamura and Hitoshi Yonehara. “Ordering of the Heisenberg Spin Glass in Two Dimensions”. In: *J. Phys. A Math. Gen.* 36 (2003), p. 10867.

[92] J. H. Mentink et al. “Stable and fast semi-implicit integration of the stochastic Landau–Lifshitz equation”. In: *J. Phys.: Condens. Matter* 22 (2010), p. 176001.

[93] B. I. Halperin and W. M. Saslow. “Hydrodynamic theory of spin waves in spin glasses and other systems with noncomnear spin orientations”. In: *Phys. Rev. B* 16.5 (1977).

[94] Daniel Podolsky and Yong Baek Kim. "Halperin-Saslow modes as the origin of the low-temperature anomaly in $NiGa_2S_4$". In: *Phys. Rev. B.* 79 (2009), p. 140402.

[95] I. Klich, S. H. Lee, and K. Lida. "Glassiness and exotic entropy scaling induced by quantum fluctuations in a disorder-free frustrated magnet". In: *Nat. Commun.* 5 (2015), p. 3497.

[96] D. M. F. van Aalten et al. "PRODRG, a program for generating molecular topologies and unique molecular descriptors from coordinates of small molecules". In: *Journal of Computer-Aided Molecular Design* 10 (1996), pp. 255–262.

[97] Jonathan Schmidt et al. "Recent advances and applications of machine learning in solid-state materials science". In: *npj Computational Materials volume* 5.83 (2019).

[98] Stefan Chmiela et al. "Towards exact molecular dynamics simulations with machine-learned force fields". In: *Nat. Commun* 9.3887 (2018).

[99] K. Mills and I. Tamblyn. "Deep neural networks for direct, featureless learning through observation: The case of two-dimensional spin models". In: *Phys. Rev. E* 97 (2018), p. 032119.

[100] K. Shiina, H. Mori, and Y. Okabe. "Machine-Learning Studies on Spin Models." In: *Sci Rep* 10 (2020), p. 2177.

[101] F. D'Angelo and L. Böttcher. "Learning the Ising model with generative neural networks". In: *Phys. Rev. Research* 2 (2020), p. 023266.

[102] A. Tanaka and A. Tomiya. “Detection of Phase Transition via Convolutional Neural Networks”. In: *J. Phys. Soc. Jpn.* 13 (2017), pp. 435–439.

[103] van Nieuwenburg, YH. E. Liu, and Huber. “S. Learning phase transitions by confusion”. In: *Nature Phys* 13 (2017), pp. 435–439.

[104] Pedro Ponte and Roger G. Melko. “Kernel methods for interpretable machine learning of order parameters”. In: *Phys. Rev. B* 96 (2017), p. 205146.

[105] Lei Wang. “Discovering phase transitions with unsupervised learning”. In: *Phys. Rev. B* 94 (2016), p. 195105.

[106] Asifullah Khan et al. “A Survey of the Recent Architectures of Deep Convolutional Neural Networks”. In: *Artificial Intelligence Review* (2020), pp. 5455–5516.

[107] Nitish Srivastava et al. “Dropout: A Simple Way to Prevent Neural Networks from Overfitting”. In: *Journal of Machine Learning Research* 15.25 (2014), pp. 1929–1958.